TAMPEREEN TEKNILLINEN YLIOPISTO
TAMPERE UNIVERSITY OF TECHNOLOGY

JOONAS HILSKA

EFFECT OF GROWTH PARAMETERS ON THE PROPERTIES OF GAASBI

Master of Science thesis

Examiner: Professor Mircea Guina
Examiner and topic approved by the Faculty Council of the Faculty of Natural Sciences
on 9th December 2015

ABSTRACT

JOONAS HILSKA: Effect of growth parameters on the properties of GaAsBi
Tampere University of technology
Master of Science Thesis, 68 pages, 0 Appendix pages
May 2016
Master's Degree Programme in Science and Engineering
Major: Advanced engineering physics
Examiner: Professor Mircea Guina

Keywords: Molecular beam epitaxy, GaAsBi

In this thesis the properties of GaAsBi structures are investigated with respect to their growth parameters in molecular beam epitaxy. The GaAsBi alloy is a novel III-V semiconductor material with many beneficial material properties, including large band gap reduction in relation to change in Bi concentration and lattice constant, which make it a promising candidate for a wide range of applications in optoelectronics. However, the progress of GaAsBi research has been hindered by challenges in its growth. Due to the weak reactivity of the Ga-Bi system, unconventional growth conditions, such as low growth temperatures and stoichiometric As/Ga flux ratios, are required for efficient Bi incorporation. Furthermore, small changes in these growth conditions induce large changes in Bi incorporation and material properties, to an extent that the poor accuracy in As flux control limits the control of material properties and reproducibility. This work aims to resolve this issue by using an unconventional growth method where the substrate rotation is stopped.

Due to the inherent spatial non-uniformity of the molecular fluxes, the stationary growth method transforms the uncertainty in As flux into spatial uncertainty of the As/Ga gradient, which can be determined accurately by ex-situ methods. Simultaneously, as the growth parameter distributions over the substrate can be determined by growth of calibration samples, the GaAsBi material properties can be examined as a function of growth conditions. This work focuses on the growth of GaAsBi bulk layers and single quantum wells with relatively high nominal Bi-fractions of around 5 %.

The Bi incorporation, structural properties and optical quality of the GaAsBi structures were found to be extremely sensitive to the growth parameters. GaAsBi grown at a low temperature of ~220 °C showed a pronounced growth window at the stoichiometric and slightly above As/Ga flux ratio range with efficient Bi incorporation, good crystal quality and smooth surfaces. At higher growth temperatures, the growth window was pinned down to only the stoichiometric range and the overall Bi incorporation was reduced. Additionally, growth at a high temperature of ~370 °C enabled efficient photoluminescence at the growth window, due to reduction in low temperature growth related defects. Interestingly, spontaneous changes in the Bi incorporation were observed at specific growth regimes, indicating fundamental growth mode changes.

TIIVISTELMÄ

JOONAS HILSKA: Kasvatusparametrien vaikutus GaAsBi-rakenteiden ominaisuuksiin
Tampereen teknillinen yliopisto
Diplomityö, 68 sivua, 0 liitesivua
Toukokuu 2016
Teknillisen fysiikan diplomi-insinöörin tutkinto-ohjelma
Pääaine: Teknillinen fysiikka
Tarkastaja: professori Mircea Guina

Avainsanat: Molekyylisuihkuepitaksia, GaAsBi

Tässä työssä tutkitaan GaAsBi-rakenteiden ominaisuuksia suhteessa niiden kasvatusolosuhteisiin molekyylisuihkuepitaksiassa. GaAsBi on uudentyyppinen III-V yhdistelmäpuolijohde, jolla on monia hyödyllisiä ominaisuuksia, kuten suuri vyöraon pieneneminen suhteessa muutokseen Bi-konsentraatiossa ja hilavakiossa, jotka tekevät materiaalista lupaavan kanditaatin moniin sovelluksiin optoelektroniikassa. GaAsBi-tutkimuksen edistystä on kuitenkin haitannut haasteet sen kasvatuksessa. Heikon Ga-Bi reaktiivisuuden ansiosta Bi:n seostaminen GaAs:iin vaatii epätavallisia kasvatusolosuhteita, kuten matalia lämpötiloja ja stoikiometrisia As/Ga vuosuhteita. Tämän lisäksi pienet vaihtelut kasvatusolosuhteissa saa aikaan niin suuria muutoksia Bi-konsentraatiossa ja materiaalin ominaisuuksissa, että huono tarkkuus As-vuon hallinnassa rajoittaa kontrollia kasvatetun materiaalin ominaisuuksista ja kasvatusten toistettavuudessa. Tässä työssä pyritään ratkaisemaan tämä ongelma käyttämällä epätavallista kasvatusmenetelmää, jossa substraatin pyörittäminen on pysäytetty. Tämä stationäärinen kasvatusmenetelmä muuttaa epävarmuuden As-vuossa näytteen pinnalle muodostuneen As/Ga gradientin paikan epävarmuudeksi. Muodostunut gradientti voidaan määrittää tarkasti kasvatuksen jälkeisillä mittausmenetelmillä. Lisäksi kasvatusparametrien jakaumat substraatin yli voidaan määrittää kalibrointinäytteiden avulla. Tällöin materiaalin ominaisuuksia voidaan tarkastella kasvatusparametrien funktiona.

Tämä työ keskittyy GaAsBi-ohutfilmien ja -kvanttikaivojen kasvatukseen, joissa As-atomeista nimellisesti n. 5 % on korvattu Bi-atomeilla. Bi-konsentraatio, rakenteelliset ominaisuudet ja optinen laatu havaittiin erittäin herkiksi kasvatusparametrien muutosten suhteen. Matalassa ~220 °C:n kasvatuslämpötilassa havaittiin selvä kasvatusikkuna stoikometrisen ja hieman ylle stoikiometrisen As/Ga vuosuhteen alueella, jossa kasvatetulla kiteellä oli tasainen pinta, hyvä kidelaatu ja täydellinen Bi-seostumistehokkuus. Korkeammilla kasvatuslämpötiloilla tämä kasvatusikkuna rajoittui pelkästään stoikiometriselle As/Ga alueelle ja Bi-seostumistehokkuus vähentyi. Toisaalta kasvatus korkeassa ~370 °C:n lämpötilassa mahdollisti korkean fotoluminesenssitehokkuuden kasvatusikkunassa johtuen kidevirheiden lukumäärän vähentymisestä. Lisäksi spontaaneja vaihteluita Bi konsentraatiossa havaittiin tarkoin rajatuissa kasvuolosuhteissa, mitkä viittasivat perustavanlaatuisiin kasvumoodin muutoksiin.

PREFACE

The research presented in this work has been carried out at the Optoelectronics Research Centre (ORC) of Tampere University of Technology. I acknowledge ORC for providing a great opportunity to study material physics of semiconductors. Although all the experimental research in this work was conducted entirely at ORC, I would like to thank all the external research groups who have collaborated with our bismide research for providing valuable information and insight. All of the MBE growth, sample processing and characterization in this work was performed by myself. Design of the sample structures and growth parameters was done by M. Sc. Janne Puustinen.

For the opportunity to work at ORC, I would like to thank Professor Mircea Guina and Dr. Tomi Leinonen. I also acknowledge Professor Mircea Guina for the supervision and examination of this thesis and Dr. Tomi Leinonen for the examination of my Bachelor's thesis. I would like to thank Dr. Pekka Savolainen for managing ORC during my studies as well as Mrs. Anne Viherkoski and Mrs. Eija Heliniemi for support with administrative tasks. The work in this thesis was financially supported by the Academy of Finland via the HIGHMAT project (No. 259111).

I would like to express gratitude to M. Sc. Janne Puustinen for his extensive work in our small but dedicated bismide team. I also acknowledge his support with this thesis. I thank both M. Sc. Janne Puustinen and B. Sc. Lauri Juhola for teaching me the basics of MBE growth and instructing me through the various characterization methods involved. I also want to thank everyone at ORC for creating a great work environment. In particular, I thank everyone in the MBE-team who have offered their help and expertise. Finally, I would like to thank my family for their support and interest in my studies.

CONTENTS

1. INTRODUCTION 1
1.1 Molecular beam epitaxy 1
1.2 Gallium arsenide bismide 1
1.3 The aim of this work 2
2. BACKGROUND 3
2.1 MBE growth 3
2.2 Low temperature MBE growth of GaAs 4
2.3 MBE growth of GaAsBi 5
2.4 Properties of GaAsBi alloys 6
3. EXPERIMENTAL METHODS 10
3.1 MBE system 10
3.1.1 Sample growth process 12
3.1.2 Flux measurement 12
3.2 Material characterization methods 16
3.2.1 High resolution X-ray diffraction 16
3.2.2 Photoluminescence 18
3.2.3 Scanning electron microscopy 21
3.2.4 Atomic force microscopy 22
4. RESULTS 25
4.1 Determination of growth parameters in stationary growth 25
4.1.1 Gallium flux 25
4.1.2 Bismuth flux 27
4.1.3 Arsenic flux 30
4.1.4 Growth temperature 33
4.2 Characterization of GaAsBi bulk layers 35
4.2.1 High resolution X-ray diffraction 36
4.2.2 Reproducibility 43
4.2.3 Scanning electron microscopy 44
4.2.4 Photoluminescence 47
4.3 Characterization of GaAsBi quantum wells 52
4.3.1 Structural properties 54
4.3.2 Photoluminescence 56
5. CONCLUSIONS 60
5.1 Future work 60

LIST OF SYMBOLS AND ABBREVIATIONS

AFM	Atomic force microscopy
AlAs	Aluminum arsenide
BAC	Band anti-crossing
BAG	Bayard-Alpert ionization gauge
BEP	Beam equivalent pressure
BSE	Backscattered electron
CBE	Conduction band edge
CHSH	Auger recombination channel
FEL	Fast entry lock
FWHM	Full width at half maximum
GaAs	Gallium arsenide
GaAsBi	Gallium arsenide bismide
GaAsN	Gallium arsenide nitride
GaSbBi	Gallium antimonide bismide
HH	Heavy-hole
HRXRD	High resolution X-ray diffraction
InGaAs	Indium gallium arsenide
IVBA	Intervalence band absorption
K-cell	Knudsen effusion cell
LH	Light-hole
LO	Longitudinal optical
LPE	Liquid phase epitaxy
LT	Low temperature
LT-GaAs	Low temperature grown gallium arsenide
LT-InGaAs	Low temperature grown indium gallium arsenide
LT-PL	Low temperature photoluminescence
MBE	Molecular beam epitaxy
MOVPE	Metalorganic vapor phase epitaxy
MQW	Multiquantum well
mVBAC	Modified valence band anti-crossing
Nd:YAG	Neodymium-doped yttrium aluminum garnet
NIR	Near-infrared
PL	Photoluminescence
QW	Quantum well
RADS	Rocking curve analysis by dynamical simulation
RT-PL	Room temperature photoluminescence
SE	Secondary electron
SEM	Scanning electron microscopy
SI	Semi-insulating
SI-GaAs	Semi-insulating gallium arsenide
SO	Spin-orbit
TEM	Tunneling electron microscopy
THz	Terahertz
UHV	Ultrahigh vacuum
VBAC	Valence band anti-crossing
VBE	Valence band edge
XRD	X-ray diffraction

A	Amplitude
BEP	Beam equivalent pressure
d	Interplanar lattice spacing
E_+	Higher energy band induced by the band anti-crossing interaction
E_-	Lower energy band induced by the band anti-crossing interaction
E_0	Primary electron energy
E_g	Band gap
F	Atomic flux
f'	Drive frequency
f_{res}	Resonance frequency
h	Planck's constant
k	Boltzmann's constant
M	Molecular weight
n	Integer
R_q	Root mean square roughness
T	Temperature
$x(T)$	Temperature dependent parameter
z	Tip-to-surface distance
α, β	Varshni fitting parameters
ΔSO	Spin-orbit splitting energy
η	Ionization efficiency
θ	Scattering angle
λ	Wavelength
ν	Photon frequency
σ	Standard deviation of localized state distribution
ω	Angle of incidence

1. INTRODUCTION

1.1 Molecular beam epitaxy

Molecular beam epitaxy (MBE) is an epitaxial growth technique where materials are deposited on a substrate in ultrahigh vacuum (UHV) conditions. MBE enables the growth of a variety of epitaxial structures with a wide range of available deposition materials, such as metals, semiconductors, oxides and even organic materials [1]. In particular, the growth of semiconductor devices, such as lasers, solar cells and transistors, is the predominant use for MBE in industry as well as research. A key attribute of MBE that allows for the production of these devices is the precision in controllability of the material composition and doping during growth. Furthermore, with MBE it is possible to grow (i) materials with low defect concentrations, (ii) well-defined interfaces and (iii) quantum structures. Owing to these properties, together with its simple working principle, MBE is well suited for the research of novel materials. [1, 2]

1.2 Gallium arsenide bismide

GaAsBi is a novel III-V compound semiconductor material which has attracted attention due to its several beneficial properties for applications. Alloying GaAs with Bi results in a large band gap reduction for only a small concentration of Bi, namely ~83 meV/% for Bi concentrations up to a few percent [3, 4, 5]. The large band gap reduction with respect to a relatively low amount of lattice mismatch [3] from GaAs makes GaAsBi very appealing in terms of wavelength extension for traditional GaAs devices, such as infrared light emitters and detectors.

Several beneficial aspects of GaAsBi arises from its band structure. The band gap reduction is mediated via a perturbation on the host valence band [6], implying that the conduction band structure and electron transport properties remain the same. Therefore GaAsBi would make an ideal material for low threshold heterojunction bipolar transistors as the threshold voltage is dependent on the band gap and high electron mobilities are required. Furthermore, the valence band is perturbed much more than the split off band, resulting in a huge spin-orbit (SO) splitting energy [7]. This makes GaAsBi a potential material for spintronic applications. In fact, the SO splitting energy is predicted to become larger than the band gap at Bi concentrations above ~10 %, which inhibits an important Auger recombination channel [8]. The suppression of Auger recombination for semiconductor lasers would result in lower threshold currents and better efficiency. Additionally, reports have shown that the band gap of GaAsBi has a better temperature tolerance than that of GaAs, which would reduce the amount of cooling needed for conventional lasers, thereby reducing their overall power consumption.

GaAsBi is also a potential candidate for terahertz (THz) spectroscopy systems. Conventional semiconductors have long (~1 ns) recombination times which hinder their use in ultrafast optoelectronic devices. However, low temperature (LT) growth of semiconductor materials has shown to reduce electron lifetimes [9]. For example, LT-GaAs [10] and LT-InGaAs [11] have been explored with limited success. Most notably, the absorption edge of GaAs (~0.9 µm) prevents the use of compact diode-pumped lasers and LT-InGaAs has low resistivity which is an obstacle for photodetector manufacture. GaAsBi, however, is typically grown at low temperatures to facilitate Bi incorporation and it exhibits similar electronic properties to LT-GaAs, namely fast recombination times and high resistivity [12]. Therefore, GaAsBi is a prospective material for near-infrared (NIR) laser activated THz emitters and detectors.

GaAsBi was first grown by Oe et al. [13] in 1998 using metalorganic vapor phase epitaxy (MOVPE) and the first reports of MBE grown GaAsBi were published in 2003 by Tixier et al. [3]. Like other explored III-V-Bi alloys, difficulties in Bi incorporation necessitated low growth temperatures and careful flux control [14, 15, 16]. The Bi incorporation and material quality sensitivity to the growth parameters has hindered the progress of GaAsBi research as the reproducibility and control of growth parameters are often insufficient for systematic GaAsBi growth.

1.3 The aim of this work

The MBE growth of GaAsBi requires careful control of growth conditions. Particularly, Bi incorporation is highly sensitive to the As/Ga material flux ratio [17], which is difficult to control accurately due to the volatile nature of the arsenic species [2]. This results in poor control of material properties and reproducibility. In this work a solution for this issue is offered by using a growth scheme where substrate rotation is stopped.

Due to the intrinsic spatial non-uniformity of the molecular beam sources [2] and the stationary substrate placement, a gradient in the incident fluxes is formed over the sample. This formed flux gradient can be determined by growing calibration structures and analyzing them with ex-situ methods, allowing for a detailed analysis of material properties with respect to these flux gradients. Particularly for the growth of GaAsBi, this growth scheme essentially transforms the uncertainty in the As/Ga flux ratio to the spatial uncertainty of the As/Ga gradient. Moreover, if the As/Ga gradient range over the substrate is larger than the uncertainty in As/Ga flux control, this spatial uncertainty will be negligible in relation to the substrate.

A study of GaAsBi material properties with respect to MBE growth parameters is presented using stationary growth. The relevant parameters for GaAsBi growth are examined and the analysis methods for each parameter are presented. Material properties with respect to the growth parameters are characterized for bulk layers as well as for quantum well structures.

2. BACKGROUND

2.1 MBE growth

The basic technique of MBE was developed in the late 1960s at Bell Laboratories by Alfred Y. Cho and John R. Arthur and the growth of GaAs by MBE was demonstrated in 1971. MBE was initially used to study semiconductor surfaces and thin films, but was quickly developed for the growth of practical optoelectronic devices. More recently however, MBE has become more common in research when compared to alternative epitaxial growth techniques, such as liquid phase epitaxy (LPE) and metalorganic vapor phase epitaxy (MOVPE). This is likely due to its superior ability to produce atomically abrupt interfaces, control the growth thickness down to monolayer precision and produce high quality semiconductor layers with precise compositions.

The working principle of MBE is straightforward. A source material is heated in a crucible in UHV (~10^{-9} mbar) conditions, causing the material to evaporate. The evaporated material passes through the crucible orifice forming a beam. The beam is then directed towards a substrate where it can adsorb to if the growth conditions, such as the growth (i.e. substrate) temperature, substrate material and other incident material fluxes, are suitable. [1]

The low vacuum pressure environment serves two purposes. First, it minimizes the incorporation of impurities into the grown material from the chamber. Impurities are often detrimental to the material electrical, optical and structural quality. To this end, the source materials and substrates must be of high purity too. Second, a low enough vacuum ensures that the mean free paths of the evaporated molecular species are longer than the dimensions of the chamber. This allows them to traverse the distance from the crucible to the substrate without interacting with each other, resulting in free molecular flow. [1]

The growth of typical semiconductor device structures requires the accurate control of numerous different material fluxes simultaneously. To achieve this, MBE systems have several independently heated material sources. Each of the sources has an individual mechanical shutter, which block the beams when necessary. The precise control of layer thickness is achieved due to the rate of closing and opening of the shutters being faster than it takes to grow a monolayer at normal growth rates. [2]

2.2 Low temperature MBE growth of GaAs

The MBE growth of high quality semiconductor materials is typically conducted using high growth temperatures. Typically, growth temperatures of ~600 °C together with high As/Ga flux ratios of over ~2 are used to grow stoichiometric GaAs thin films with excellent optical, structural and electrical properties. At these growth conditions, the Ga flux controls the growth rate due to its unity sticking coefficient and negligible desorption from the growth surface. The more volatile As species sticking coefficient is highly dependent on the available group V site concentration on the growth surface, allowing all excess As to desorb. Due to the high surface diffusion rate of Ga, growth of stoichiometric crystalline GaAs is achieved. [2]

Beyond the typical growth of GaAs, unconventional growth conditions are often required to alloy other materials with GaAs. This is the case for GaAsBi [3] and GaAsN [18], for example. To understand the growth and properties of these ternary alloys, it is necessary to understand the growth and properties of the base binary system grown at similar conditions.

Low temperature grown GaAs has been studied extensively due to its unique properties. Reducing the growth temperature below ~400 °C and using above unity As/Ga flux ratios, excess arsenic can incorporate into the lattice forming native point defects [19, 20]. The defects are predominantly As_{Ga} antisites and V_{Ga} vacancies, although some negligible amounts of As_i interstitials are formed also [19]. These native point defects can act as fast recombination centers. Subsequently, thermally annealing the non-stoichiometric LT-GaAs layer forms nanoscale As clusters making it highly resistive. Despite the high density of point defects and As clusters, the carrier mobility in the material is relatively high, making it ideal for fast photoconductor devices [10].

The concentration of the point defects depends on both the growth temperature and the As/Ga flux ratio. When increasing the As/Ga flux ratio above stoichiometric (equal As and Ga atomic fluxes) conditions, the concentration quickly rises and eventually saturates to a constant value [20, 21, 22]. When increasing the growth temperature at above stoichiometric As/Ga conditions, the concentration decreases approximately linearly (based on the data presented in references [19] and [20]). Using high As/Ga ratios and low temperatures, highly nonstoichiometric GaAs layers with ~1 % excess As can be achieved [19, 20]. Nonetheless, the layers still possess high crystalline quality with only a small deviation from the stoichiometric GaAs lattice constant, which is proportional to the concentration of the As_{Ga} antisites [19, 21, 22].

It should be noted, that the growth regime where below stoichiometric As/Ga flux ratios are used for LT-GaAs growth remain relatively unexplored. The use of this As limited growth mode results in the accumulation of excess Ga as metallic surface droplets [2]. Moreover, even at near stoichiometric As/Ga flux ratios, the surface quality deteriorates

due to the limited surface diffusion of Ga at low temperatures. The point defects formed under this growth regime are not known. However, LT-GaAs grown near stoichiometric conditions is lattice matched to stoichiometric GaAs [20], implying that the As_{Ga} defect concentration is suppressed.

2.3 MBE growth of GaAsBi

The Bi incorporation into GaAs requires very unusual growth conditions due to the weak reactivity of the binary Ga-Bi system. In fact, the Ga-Bi phase diagram shows no stable (solidus) compounds of Ga-Bi for any temperature or composition [23]. This, together with the large size of the Bi atom and the strong tendency of Bi to surface segregate, makes the growth of GaAsBi challenging. Although GaAsBi was first grown by MOVPE, MBE is generally the preferred method due its non-equilibrium growth mechanism which allows for the growth of metastable alloys like GaAsBi.

Generally speaking, Bi incorporation depends on three different growth parameters: growth temperature, As/Ga flux ratio and Bi flux. To achieve efficient Bi incorporation, growth temperatures of below ~400 °C, As/Ga flux ratios near or below unity and low Bi/Ga flux ratios are required [3, 24].

Due to the weak bonding of Ga-Bi, low growth temperatures must be used to prevent Bi evaporation from the growth surface. Additionally, the low growth temperatures inhibit the surface segregation of Bi from the bulk layer to the surface. Growth temperatures as low as ~200 °C can be used to maximize Bi incorporation [17]. However, the tradeoff for lower growth temperatures is the onset of low temperature growth related defects and inferior surface quality, as mentioned in chapter 2.2.

Bi incorporation is highly sensitive to the As/Ga flux ratio. This is due to the nature of Bi being fully substitutional in the GaAsBi alloy [25, 26], making As and Bi atoms compete for the available group V sites [3, 24]. Low As/Ga flux ratios are therefore required for Bi incorporation, namely near or below stoichiometric values. At these conditions, however, the surface quality of the layers are deteriorated by either reduced surface diffusion rates of Ga or the onset of metallic Ga or Ga/Bi compound droplets [27, 28]. To achieve smooth surfaces required for device manufacture, slightly above stoichiometric values must be used. However, when increasing the As/Ga flux ratios above the stoichiometric value, the Bi incorporation is quickly suppressed [17].

Bi incorporation is approximately linearly proportional to the Bi flux or, more accurately, the Bi/Ga flux ratio when using stoichiometric As/Ga flux ratios and low Bi/Ga flux ratios [17, 29]. However, the Bi incorporation does eventually saturate at high Bi/Ga values leading to Bi droplet formation [17]. For example, in one particular experiment using varying growth rates, the Bi concentration showed no saturation up to ~12 % [29].

To date, the highest achieved Bi concentration in GaAs is reported to be 22 % [17]. This was achieved by using a very low growth temperature of 200 °C, a below stoichiometric As/Ga flux ratio and a high Bi/Ga flux ratio. Although these growth conditions resulted in Ga and Bi droplets on the surface, the layer showed moderately good structural quality. The optical quality of the layer was not reported, but it can be expected to be severely degraded due to the low growth temperature and below stoichiometric As/Ga ratio used. The current record for highest Bi concentration layer with good optical quality (showing photoluminescence at room temperature) is 10.8 %, equivalent to a wavelength of 1.52 μm [30].

Although the fundamental MBE growth parameters affecting Bi incorporation are outlined here, a complete model for GaAsBi growth is yet to be established. The current most comprehensive model was established by Lewis et al. [17] which was developed from earlier work by Lu et al [24]. Despite showing excellent agreement with experimental data between Bi incorporation and growth parameter values, this model has not yet addressed the growth of optimal quality GaAsBi at any composition. Additionally, other relatively unexplored growth parameters, such as the choice of As species [31], growth rate [29] and crystal growth plane [32], have been shown to affect Bi incorporation properties. The sensitivity of material properties with respect to the growth parameters and the interplay between these parameters makes GaAsBi growth challenging.

2.4 Properties of GaAsBi alloys

Alloying GaAs with Bi leads to an anomalously large band gap bowing. Band gap reduction values of ~83 meV/% for dilute Bi concentrations of a few percent have been generally reported [3, 4, 5, 7], although some have reported values as low as 42 meV/% [33]. The current understanding of the band structure of GaAsBi is explained by a modified form of the valence band anti-crossing [(V)BAC] model, referred to as mVBAC.

The BAC model was initially developed for III-V and II-VI semiconductor alloys where highly electronegative isoelectronic impurity atoms were incorporated into the anion sub-lattice, as is the case for GaAsN, for example. In the BAC model, the impurity atoms induce localized defect states near the conduction band edge (CBE). These defect states go through an anti-crossing interaction with the conduction band, causing it to split into two levels, E_- and E_+, which are offset from the original CBE, namely the E_- moving downward leading to the band gap bowing. Correspondingly, the VBAC model considers a similar process for the valence band.

In the case of GaAsBi, Bi introduces localized states (due to its large size and low ionization energy) near the valence band edge (VBE). This is corroborated by the p-type conductivity of nominally undoped GaAsBi [34]. Initial theoretical work by Alberi et al. [35] suggested that these localized states then go through an anti-crossing interaction with all of the valence bands, creating heavy-hole (HH), light-hole (LH) and SO vari-

ants of the E_- and E_+ levels. The lifting of the HH and LH related E_+ levels from the original VBE would then lead to the band gap bowing of GaAsBi. More recently however, this model was found to overestimate the band gap of GaAsBi for high Bi fractions [30]. This discrepancy has been since resolved by the mVBAC model, where the BAC interaction only affects the HH/LH bands and the SO and CBE bands are understood with conventional (i.e. linear dependency on composition) alloying effects [6].

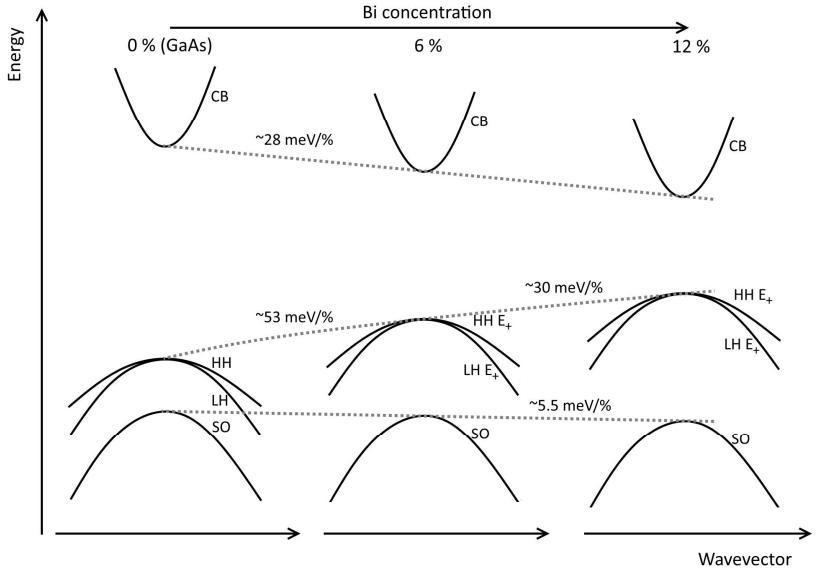

Figure 2.1 A simplified schematic of the mVBAC model. Adapted from reference [6].

The mVBAC shows excellent agreement with experimental data for the GaAsBi band gap and SO splitting energy for Bi concentrations up to ~10 % [36]. The band gap is reduced due to a linear ~28 meV/% reduction in the CBE energy while the top-most E_+ related levels increase by ~53 meV/% at low Bi concentrations and ~30 meV/% at high Bi compositions [6]. The SO band reduces slowly at ~5.5 meV/% resulting in the SO splitting energy exceeding the band gap energy at Bi concentrations above ~10 %. At these Bi concentrations an important Auger recombination channel is suppressed (see Figure 2.2) in which a conduction band electron recombines with a HH, in turn, exciting a SO split-off band hole to the HH band (referred to as the CHSH channel). Similarly, intervalence band absorption (IVBA), i.e. the optical transitions from the SO split-off to the HH or LH band, would be suppressed. These two processes are the dominant loss mechanisms in telecommunication devices.

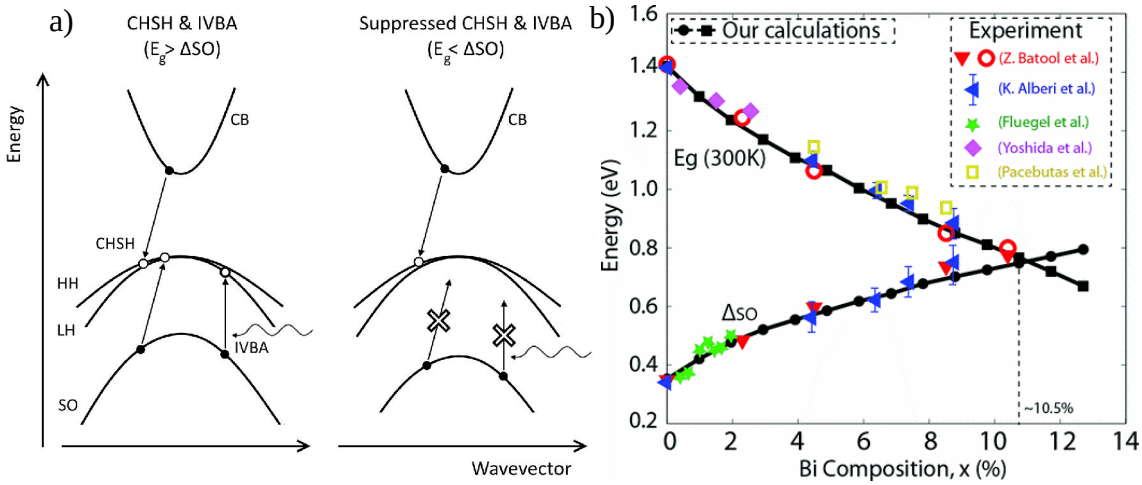

Figure 2.2 a) Illustration of suppression of the CHSH Auger recombination channel and the IVBA process due to the SO splitting energy exceeding the band gap energy. b) Band gap and SO splitting energy values as a function of Bi concentration (reprinted with permission from reference [6], "Our calculations" refers to tight-binding calculations conducted by the corresponding authors).

Apart from the large bowing, the band gap of GaAsBi has been reported to show improved temperature tolerance compared to GaAs. Pioneering work by Oe et al. [13] reported a thermal coefficient as low as -0.1 meV/K. However, others have since reported thermal coefficients of -0.4 meV/K [4] and -0.35 meV/K [37], which are almost identical to that of GaAs. Tominaga et al. [38] showed that the temperature dependence for GaAsBi multiquantum wells (MQWs) decreased with increasing Bi concentration. Recently, Pettinari et al. [39] contributed similarly by showing the same compositional trend for the thermal coefficient of bulk GaAsBi for Bi concentrations up to 10.6 %. These two results are comprised in Figure 2.3.

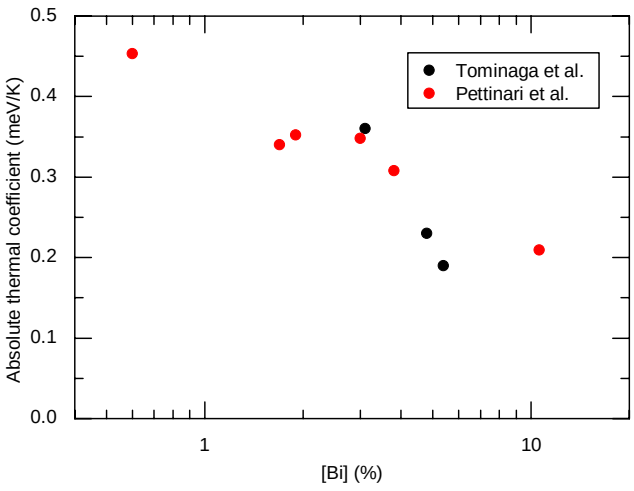

Figure 2.3 Absolute thermal coefficient values as a function of Bi concentration. Adapted from references [38] and [39].

The electrical properties of GaAsBi are reflected by the changes of band structure induced by the Bi incorporation. The electron mobility remains unchanged from GaAs for dilute amounts of Bi up to ~1.4 % [40, 41]. At higher concentrations some degradation is observed, but no clear compositional trend is seen which might indicate the degradation is due to poor growth optimization, rather than changes in the conduction band. The hole mobility decreases with increasing Bi concentration [34, 42, 43]. However, the degradation is modest in comparison to the dramatic electron mobility decrease of GaAsN with increasing N concentration [43].

Bi incorporation in GaAs is fully substitutional [25, 26], i.e. the Bi atoms incorporate into the group V (i.e. As) face-centered cubic sub-lattice of the zincblende matrix. Due to the large size of the Bi atoms compared to As, the GaAs lattice expands with increasing Bi concentration. Vegard's law describes this expansion for typical ternary compounds by a linear combination of the binary constituents' lattice constants. For GaAsBi however, the theoretical compound GaBi has not been successfully synthesized so its lattice constant must be approximated. An estimate of 6.33 Å has been reported based on extrapolating the linear lattice expansion of GaAsBi as a function of Bi incorporation [3]. This value agrees with a theoretical estimate of 6.32 Å [44].

In addition to the aforementioned alloy properties, GaAsBi has been shown to have several interesting microstructural properties. Alloy disorder-related features have been observed in power and temperature dependent photoluminescence measurements, which have been attributed to existence of localized states induced by Bi clustering [45]. The atomic clustering of Bi has been directly observed by tunneling electron microscopy (TEM) [46]. Additionally, atomic ordering, such as triple-period [47] and CuPt-type [48] ordering, have been observed in GaAsBi layers by TEM. Recently, larger scale modulation of the Bi composition was reported, where the Bi composition varied laterally across the GaAsBi layer forming columnar-like nanostructures [49]. This intrinsic tendency for phase separation has also been apparent in thermally annealed GaAsBi layers, where Bi self-organizes into Bi-rich nano-clusters [50].

3. EXPERIMENTAL METHODS

3.1 MBE system

The samples in this work were grown in a VG V80H MBE system, which is a model often used for research purposes. The system has been configured for III-V epitaxy and has material sources for Al, Ga and In as well as N, As and Bi for the group III and V species, respectively. Additionally, Si and Be sources are equipped as n- and p-type dopants, respectively. The group III and dopant sources, along with Bi, are traditional Knudsen effusion cells (K-cell), whereas the remaining group V sources are specially designed sources. The K-cells are simple thermal evaporators where the source material is heated in a crucible to a melt and the amount of material flux is controlled by careful regulation of the cell temperature. Excluding As, the source beams are turned on and off with individual mechanical shutters which are pneumatically controlled.

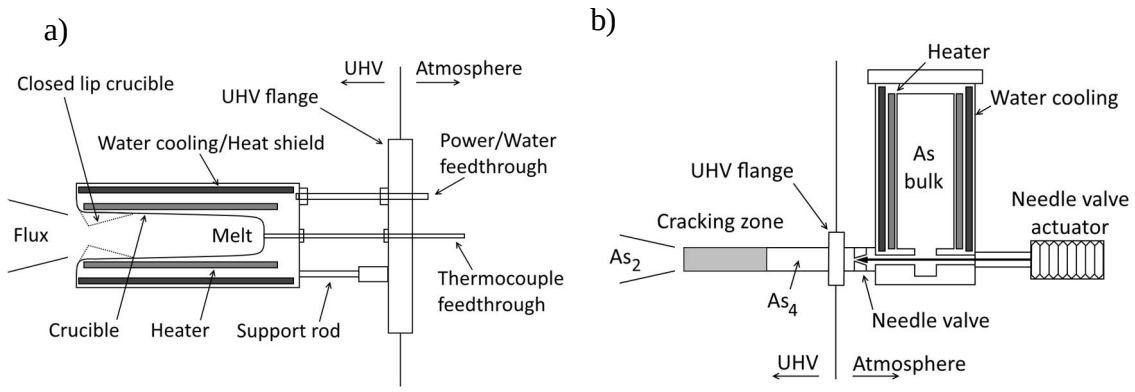

Figure 3.1 Cross-sectional schematics of a) a K-cell and b) a valved cracker cell.

As is supplied by a valved cracker cell. It comprises two segments: a bulk stage and a cracker stage. In the bulk stage, As is heated in a crucible resulting in the evaporation of As_4 molecules. The As_4 molecules then pass through a needle valve to the cracking stage, which can be heated to thermally dissociate the As_4 tetramers into As_2 dimers. The As source therefore has two operating modes based on the cracking zone temperature: a lower temperature mode allowing the As_4 to pass through and a high temperature mode producing As_2. In this work, only the As_2 mode is used. The As material flux is controlled by a combination of the bulk stage temperature and the needle valve position.

A plasma source for N is fitted to the reactor. The material flux is controlled by a mass flow controller and a mechanical shutter. However, the specifications for this source are omitted here, as it is not used in this work.

The MBE system comprises three vacuum chambers: the fast entry lock (FEL) chamber, the preparation chamber and the growth chamber. Each of these chambers have individual pumping systems and are separated with vacuum valves. Exchange of substrates and grown samples between the system and atmospheric conditions happens via the FEL chamber. The FEL chamber can be quickly vented to atmospheric pressures by filling the chamber with pure nitrogen while keeping the vacuum pumps off. After reaching atmospheric pressures, the previously grown sample can be taken out from their wafer holding block and a new substrate can be put in. The block, which is made of molybdenum due to its thermal stability and inertness, holds the wafer in place gravitationally in a grooved opening which follows the edge of the wafer. The FEL chamber accommodates several of these blocks in a cassette. After the exchange process, the FEL chamber is pumped down by a turbomolecular pump together with its diaphragm backing pump. After reaching ~10^{-7} mbar vacuum level, the new substrate in its block can be moved to the preparation chamber where it's heat treated to promote the outgassing of impurities, such as water, alcohols and atmospheric particles. The preparation chamber is pumped by an ionization pump and the vacuum levels are typically ~10^{-8} mbar.

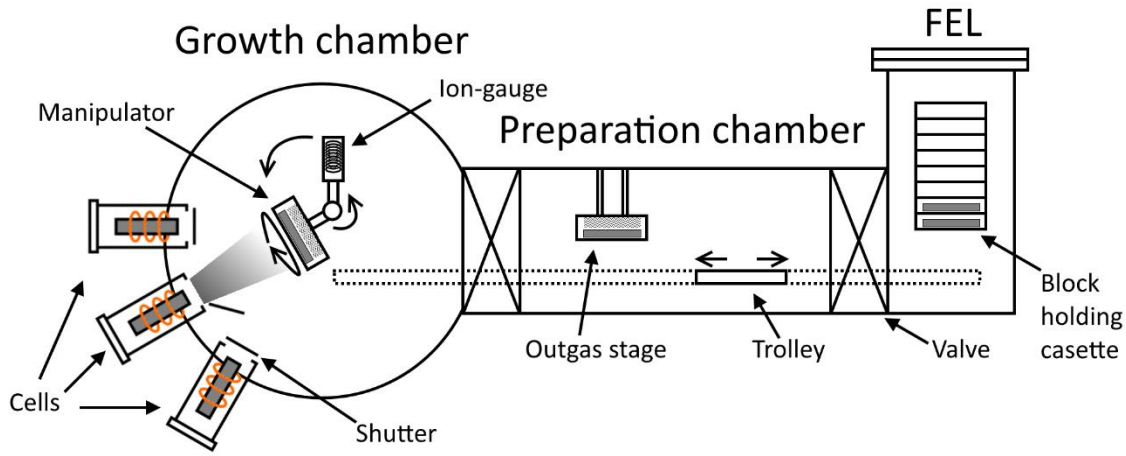

Figure 3.2 Schematic cross-section of the MBE system used in this work.

After sufficient heat treatment, the substrate can be moved to the growth chamber. The growth chamber has the best pumping capability. It pumped by a diffusion pump together with a liquid nitrogen-filled cryopanel surrounding the chamber. Additionally, an ionization pump and a titanium sublimation pump are fitted. The diffusion pump is backed by two rotary vane pumps. When cells are at idle temperatures, vacuum levels of ~10^{-10} mbar can be reached.

The blocks can be moved inside the chambers by wobble sticks. They consist of a magnetically actuating arm, which mimics the movements made on the handle outside the chamber, with a spatula that attaches to the blocks via an upright facing pin. Furthermore, a mechanical trolley mechanism enables the transfer of blocks between the three chambers.

3.1.1 Sample growth process

A standard pre-growth processing is required to ensure comparability between the grown samples and to be able to reproduce the grown structures. The growth of every sample is preceded by the same heat treatment in the outgassing stage, which is set to a temperature of ~300 °C (thermocouple estimate). When inserting the sample in the stage, impurities start to evaporate from the sample surface causing the pressure in the preparation chamber to rise. Over a span of a few minutes, the pressure in the chamber reaches a maximum level and begins to decrease. The maximum pressure level is typically in the range of 10^{-8} – 10^{-6} mbar and depends on the cleanliness of the substrate and block. When the pressure level has decreased below a standardized value of 2×10^{-8} mbar, the wafer is transferred to the growth chamber. The duration of the heat treatment is typically two to three hours.

In the growth chamber, the sample is placed into the manipulator arm. The manipulator has a similar heating system to the outgassing stage and its temperature is kept at a temperature of ~320 °C. The temperature of the substrate (here referred to as growth temperature or T_g) is monitored by a pyrometer and a thermocouple. Due to the thermocouple being mounted to the back of the substrate and not having direct contact with the substrate, the actual substrate temperature can deviate by several tens of degrees from the thermocouple reading. Therefore, the substrate temperatures in this work are estimated from a linear extrapolation of pyrometer and thermocouple values from the high temperature range where the pyrometer reading is the most accurate.

The growth of every sample is initiated by a heating sequence and starting sample rotation, which is kept at roughly ~18 rpm during growth to ensure uniform flux distribution over the wafer. The heat sequence must be performed to remove the native oxide layer and any remaining impurities that were not removed by the outgassing. The sample is heated to ~620 °C in two stages and kept at this temperature for 10 min. During this sequence, the As valve is kept open to provide an As overpressure which prevents arsenic desorption and subsequent surface degradation. After the heat sequence, the sample temperature lowered to an optimal GaAs growth temperature of ~580 °C while still having the As valve open. A ~150 nm GaAs buffer layer is grown with a high As/Ga flux ratio on the substrate to ensure a smooth and clean surface on top of which the actual structure being studied is grown.

Due to the variety of sample structures grown for this work, the detailed growth parameters of each sample are presented in the results chapter.

3.1.2 Flux measurement

Nude Bayard-Alpert ionization gauges (BAG) are used for measuring the magnitude of the molecular beam fluxes as well as chamber pressure monitoring. The working princi-

ple of BAGs is very simple and they consist of only three components: a filament (cathode), a grid (anode) and an ion collector (ground). A schematic drawing of a nude BAG is provided in Figure 3.3. The filament is heated by driving current through it and it begins to emit electrons. The emitted electrons are then accelerated towards the positively charged grid, where most of the electrons pass through to the space enclosed by the grid. In this space, the electrons ionize a fraction of the gas molecules by collisions. The formed positively charged ions are then collected efficiently by the grounded ion collector which is connected to an electrometer. The current generated at the ion collector is thereby proportional to the amount of gas molecules inside the grid and thereby proportional to the flux passing the grid. For molecular beam flux measurements, the raw current value is often referred to as the beam equivalent pressure (BEP) by convention.

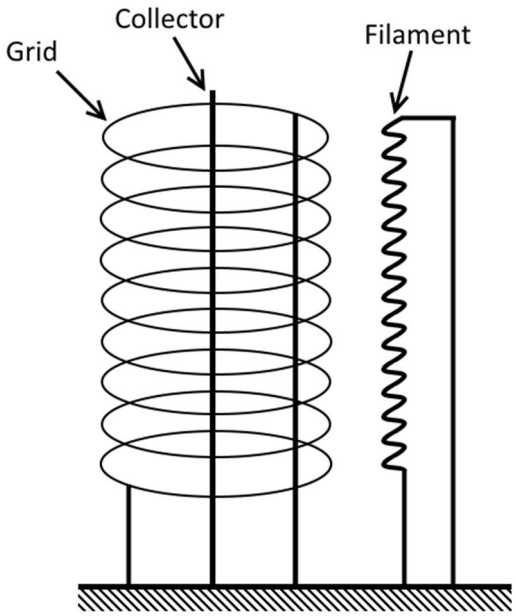

Figure 3.3 Schematic of a Bayard-Alpert ionization gauge.

In literature absolute BEP values are typically unreported. This is due to them being dependent on multiple factors, some of which are specific for the BAG model used. Most notably, the ion gauge sensitivity, geometry of the grid and ionization efficiency of the molecular species factor in to the absolute BEP value measured. Therefore, BEP values are often converted to flux ratios by equation 3.1.

$$\frac{F_X}{F_Y} = \frac{BEP_X \eta_Y}{BEP_Y \eta_X} \left(\frac{T_X M_Y}{T_Y M_X}\right)^{1/2} \qquad 3.1$$

Equation 3.1 relates the BEP value ratio for two different molecular species X and Y to the flux value F ratio using the ionization efficiency η, absolute source temperature T and molecular weight M. Alternatively, BEP values are converted into absolute flux values by using in-situ measurement methods or ex-situ characterization of different calibration samples.

The flux measurement BAG in the system is mounted on to the backside of the manipulator arm as depicted in Figure 3.2. During flux measurement, the arm is rotated in such a way that the BAG is directly on the molecular beam paths. The measurement process for each flux species depends on their tendency to adsorb to surfaces present in the chamber. Generally speaking, measurement of group III species is straightforward as they tend to stick to the first surface they meet in the chamber. This means that the beam passes through the BAG grid only once and then adsorbs to the backside of the manipulator and chamber walls, making the molecular flux and thereby BEP value stable over time. However, for the more volatile group V species this is not the case.

Group V species, such as As_2 and As_4, tend to have a lower probability of sticking to the chamber walls. This results in the beam reflecting off the surfaces behind the BAG and making a second pass through the grid. This, in turn, leads to a gradual BEP increase over time and, due to the sticking coefficients being essentially unknown for these different surfaces, renders the measurement useless. This issue is circumvented by depositing a coating on the surfaces behind the BAG for which the sticking coefficient of the species being measured is unity. This way, all the group V species initially stick behind the surfaces of the BAG and a measurement can be made that is a representative of the incident flux. However, this initial condition is only temporary as the incident group V species start saturating the available adsorption sites on the coating, resulting in a BEP rise. The deposition of group III species, such as Ga, Al or In, is typically used as the coating. Due to the transient nature of the sticking coefficient in this process, the accuracy for group V BEP measurements is poor. An accuracy of ~10 % is achieved in measuring As_4 BEP with a 60 second Ga pre-deposition at typical As_4/Ga flux ratios, whereas group III BEPs can be determined with an accuracy of ~0.5 % [2].

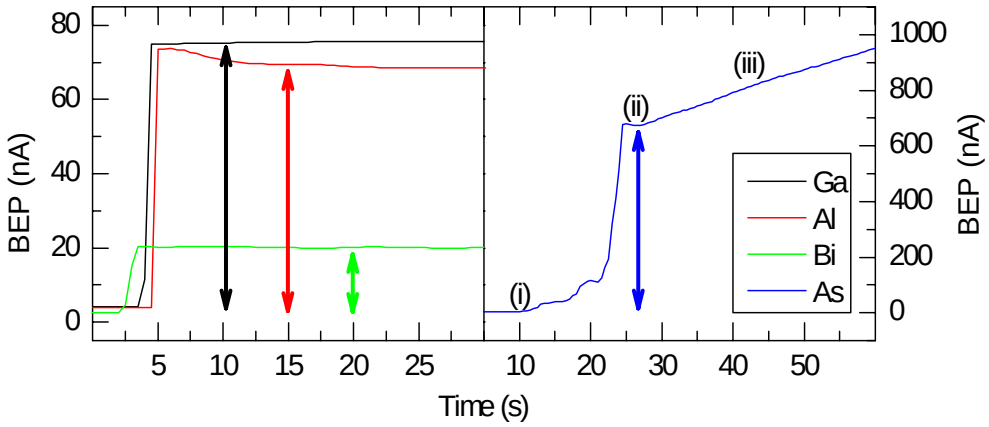

Figure 3.4 Examples of typical BEP measurements for Ga, Al, Bi and As. The double-headed arrows show the approximate recorded BEP values. The right hand side graph indicates the (i) valve jog start, (ii) As unity sticking coefficient transient and (iii) increase of the BEP value due to reflection. The initial decrease in the Al BEP curve is likely caused by thermal instability of the cell due to opening the shutter.

In this work the BEP measurements were conducted in a standardized fashion. Al was measured first by opening the shutter and recording the BEP for 3 min. After this, the shutter was closed and the background BEP was measured for 1 min. The Al BEP was recorded as the averaged (temporal mean from the stabilized BEP curve at the back end of the measurement) Al BEP subtracted by the average background BEP. Second, Bi was measured (if used for the following growths) using the same process. It is noted here, that the previous Al measurement was sufficient as a coating, evidenced by the stable Bi BEP curve in Figure 3.4. Next, the Ga BEP was recorded by averaging three sequential measurements using measurement times of 30 s and 15 s for the Ga BEP and background, respectively. Finally, the As BEP curve was measured for 1 min at five specific needle valve openings with each measurement being preceded by an Al deposition of 2 min. The needle valve was opened gradually to the respective valve positions using a constant acceleration rate mode of the linear actuator (referred to as jogging). The transient unity sticking coefficient values of the As BEP curve, shown in Figure 3.4, were recorded manually as a function of the needle valve position, shown in Figure 3.5.

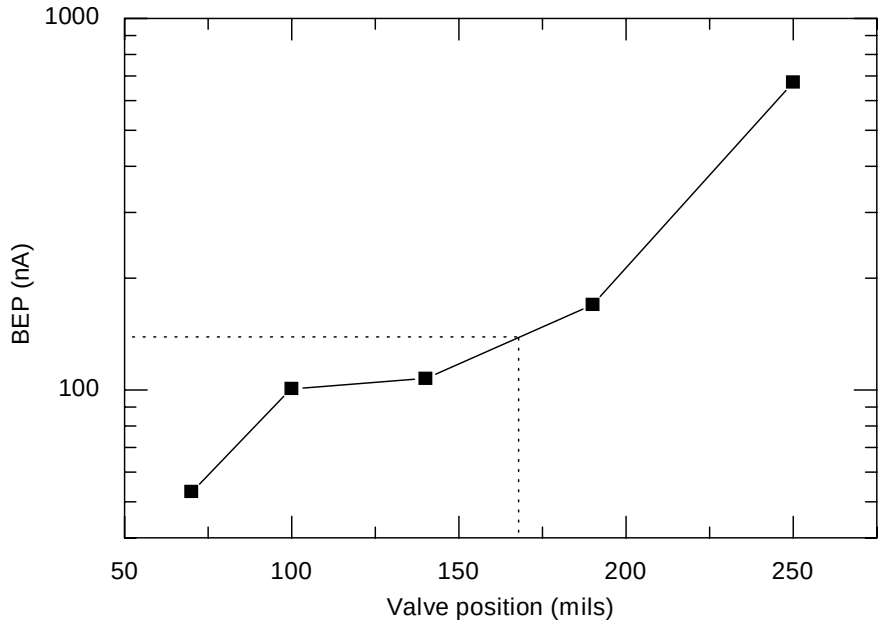

Figure 3.5 As BEP as a function of the needle valve position. The dashed line indicates the method of interpolating a specific valve opening value corresponding to a target As BEP.

An important observation from the systematic flux measurement over a long period of time is that the As BEP tends to have much more erratic behavior than the typical group III species. Specifically, the simpler K-cells show a generally monotonous decrease in material output over time at constant cell temperature due to material consumption, whereas the more complex As source setup shows occasional increases in output at constant source temperature. This unpredictable behavior, and the cumulative effect of the

inaccuracy in As BEP measurement together with the interpolation method used to determine target As flux values, elucidates the challenge in growth of GaAsBi, as the control of As flux is critical in terms of resulting material properties.

3.2 Material characterization methods

3.2.1 High resolution X-ray diffraction

X-ray diffraction (XRD) techniques are versatile tools in the study of crystallographic structure of materials. In XRD, a material is subjected to a collimated beam of X-rays. The X-rays interact with the atoms' electronic clouds each of them re-radiating a spherical wave with the same frequency as the incident wave. If the atoms are arranged in a regular array, i.e. they form a crystalline structure, the spherical waves can constructively interfere in a few specific directions, determined by Bragg's law (equation 3.2).

$$2d \sin\theta = n\lambda \qquad 3.2$$

In equation 3.2, d is the spacing between the crystal lattice planes, θ is the incident angle with respect to the diffracting lattice plane, n is an integer and λ is the wavelength of the X-rays. Due to the X-ray wavelength being comparable to the lattice plane spacing, a diffraction pattern can be observed when scanning through a range of incidence angles. Based on the angles corresponding to intensity maxima, the lattice plane spacings can be calculated using Bragg's law.

In high resolution X-ray diffraction (HRXRD), a small angle range around a single diffraction maximum is measured with high angular resolution. The aim of this measurement is to detect slight deviations from the ideal crystal structure, which would result in a slight deviation in the diffraction maximum position (here referred to as simply mismatch). The detection of these deviations is particularly useful for the analysis of thin films, as the epitaxial layers are typically slightly lattice mismatched from the substrate. For example, a thin epilayer with a slight lattice mismatch from the substrate forms an additional diffraction peak next to the substrate diffraction maximum. Moreover, a ternary epilayer's composition or, in very specific cases, the epilayer's defect concentration can be determined accurately, due to the lattice mismatch being proportional to these quantities. Even the epilayer's thickness can be determined by analyzing the Pendellösung fringes (colloquially referred to as thickness fringes) around the secondary peak. Subsequently, structural inhomogeneity or interfacial quality can be qualitatively assessed if these features are deteriorated. Additionally, relaxation of the epilayer can be quantitatively measured by reciprocal space mapping.

Detailed quantitative information from the HRXRD diffractogram is gained by fitting a simulated model to the measured data. This is firstly due to the complexity of the features produced by structures other than single epilayers. Secondly, it has been shown

that a straightforward peak mismatch analysis can lead to errors for single epilayers with thicknesses below ~1–2 µm [51]. In this work the simulations are done with Bede RADS software, which uses a dynamical theory of X-ray diffraction based on the Takagi-Taupin equations. Figure 3.6 depicts a measurement and a corresponding simulation of two a typical structure grown for this work.

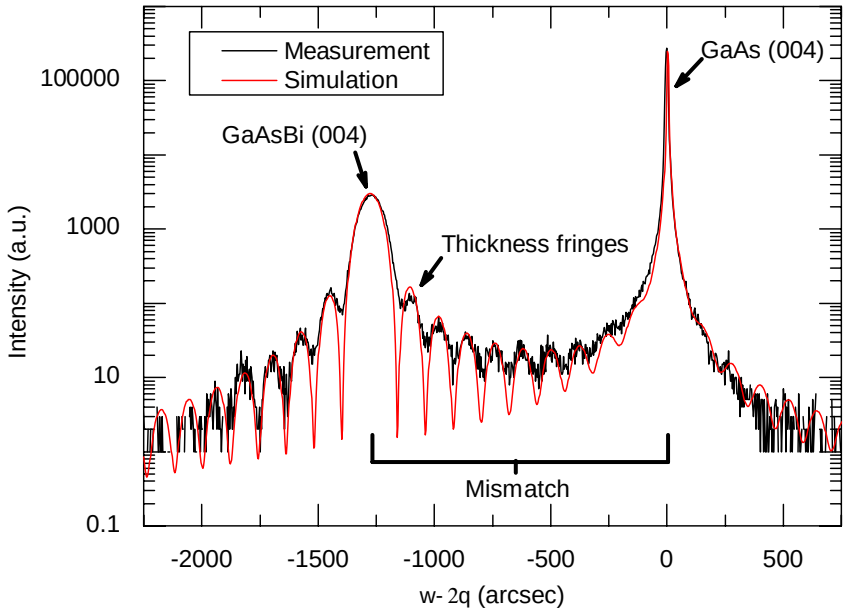

Figure 3.6 Example of a HRXRD measurement fitted with a RADS simulation of a GaAsBi epilayer grown for this work (thickness ~160 nm and [Bi] ~4 %). The ω-2θ axis is centered to the diffraction maximum corresponding to the GaAs(004) planes.

The HRXRD measurement system used in this work is the Phillips X'Pert PRO materials research diffractometer. The X-rays are generated in a ceramic high power X-ray tube with a Cu anode, which provides Cu K-alpha (0.154056 nm) radiation with a long fine focus. To condition the X-ray beam, an X-ray mirror together with a four crystal Ge(220) monochromator are used. The system also has a crossed slits assembly mounted to the end of the monochromator to control the beam dimensions. To maximize the incident X-ray intensity, the assembly slits were left fully open, so the beam dimensions were determined by the mirror and monochromator apertures. The measured beam dimensions are approximately ~1.8 mm in width and ~14 mm in height when hitting the sample, which is mounted onto a triple-axis goniometer. The diffracted intensity is collected by a proportional detector consisting of a cylindrical chamber filled with a xenon/methane mixture. An analyzer provides a narrow detection range of 12 arcseconds by having the diffracted beam undergo three Ge(220) reflections. The geometry of the experimental setup is shown in Figure 3.7.

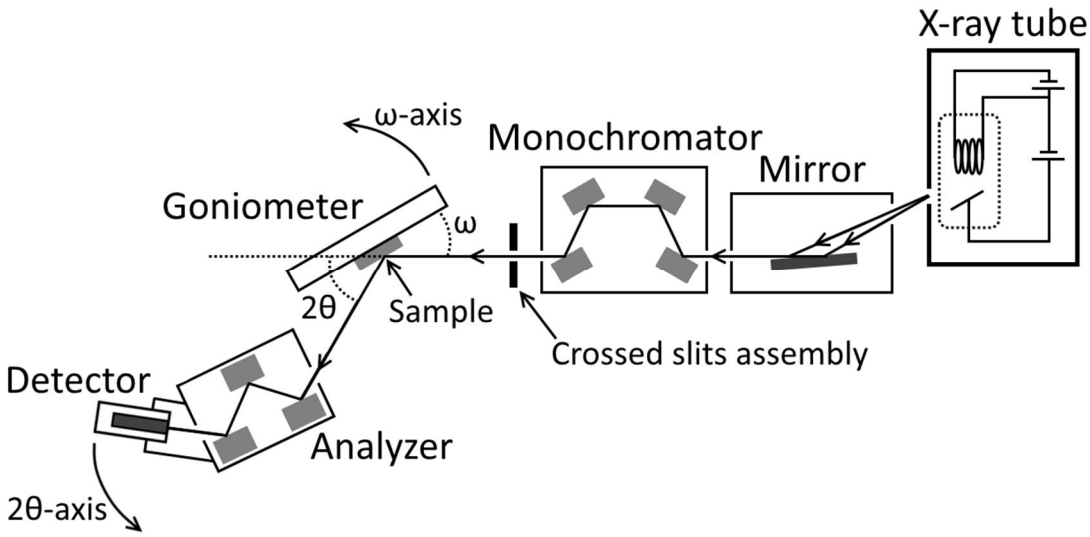

Figure 3.7 Schematic of the experimental setup showing the optical path of the X-ray beam.

The HRXRD measurements in this work are so called ω-2θ triple-axis coupled scans. In these scans both of the ω- and 2θ-axis, shown in Figure 3.7, are rotated simultaneously with the 2θ-axis being moved with twice the angular velocity. Using a symmetric scan (i.e. $\omega = \theta$), the mismatched Bragg peaks are observed for the epilayers parallel to the substrate. Specifically, the diffraction maximum corresponding to the GaAs(004) lattice planes is measured over. This is due to its high structure factor, which governs the maximum diffraction intensity.

3.2.2 Photoluminescence

Photoluminescence (PL) is light emission from a material that has been excited with photons. The absorption of the exciting photons in a material results in various relaxation processes in which other photons can be re-radiated. The material can be characterized by the energy distribution of these re-radiated photons (i.e. PL spectrum), as the energies are dependent on the excited material's electronic structure.

PL spectroscopy is a powerful tool in semiconductor characterization, as it gives information about the band gap energy as well as defect states. In a PL measurement, the sample gets excited by photons with energies larger than the band gap. Typically, the incident photons are produced by a focused monochromatic laser. The incident photons excite electrons from the valence band of the semiconductor to the conduction band. Correspondingly, holes in the valence band are formed. The excited electrons and holes then rapidly thermalize to the band edges by creating lattice phonons. At the band edges, the electron and hole recombine in various processes either radiatively or non-radiatively.

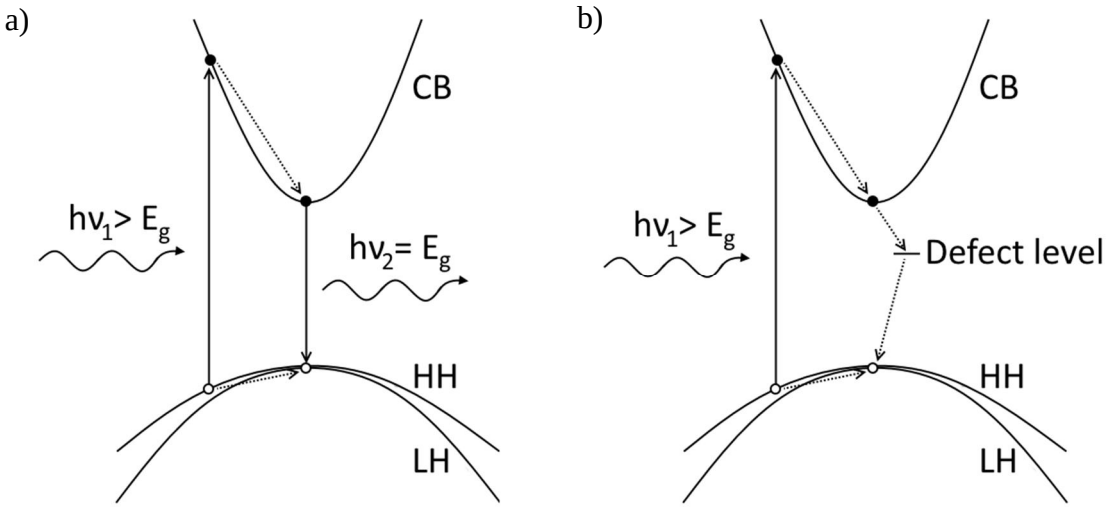

Figure 3.8 a) Radiative band edge recombination. b) Non-radiative recombination mediated by a mid-gap defect level.

The relaxation processes are governed by band structure and defects. Energy and momentum must be conserved in the processes by either carrier, photon or phonon excitation. Phonon excitation is typically the dominant momentum conservation mediator, due to the negligible momentum of photons corresponding to typical semiconductor band gap energies. Therefore, for direct band gap semiconductors, where momentum transfer is negligible due to the valence band maximum coinciding with the conduction band minimum in momentum-space, a photon mediated band-to-band relaxation process dominates resulting in good PL efficiency. Conversely, for indirect band gap semiconductors, conservation of momentum is mediated by phonons making photon emission a second order process, resulting in worse PL efficiency. Carrier mediated recombination, referred to as Auger recombination, dominates at high carrier concentrations, due to the requirement for secondary carriers to be excited. Defects, such as impurities or lattice imperfections, introduce electronic states within the band gap, through which electrons and holes can relax either radiatively or non-radiatively, altering the PL efficiency and spectrum.

In this work the room temperature PL (RT-PL) measurements were carried out with the Accent rapid photoluminescence mapper 2000 system. The excitation source in this system was a 532 nm Nd:YAG continuous wave laser with a maximum power density of ~1000 Wcm^{-2}. The PL signal is filtered by a longpass filter (570 nm, to block the exciting laser wavelength) and a monochromator before being collected by an InGaAs detector.

The low temperature PL (LT-PL) measurement system was custom built on top of an optical table. A schematic of the system is depicted in Figure 3.9a. For excitation, a laser diode with emission wavelength of 690 nm was used, which was capable of producing a maximum power density of ~100 Wcm^{-2}. A lock-in technique was used to amplify

the weak signal detected by the thermoelectrically cooled InGaAs detector, which provides an efficient spectral response for the NIR range. The closed-cycle He cryostat was capable of reaching ~10 K. An example measurement is provided in Figure 3.9b of a semi-insulating (SI) GaAs sample, which was the chosen substrate material for all grown samples in this work.

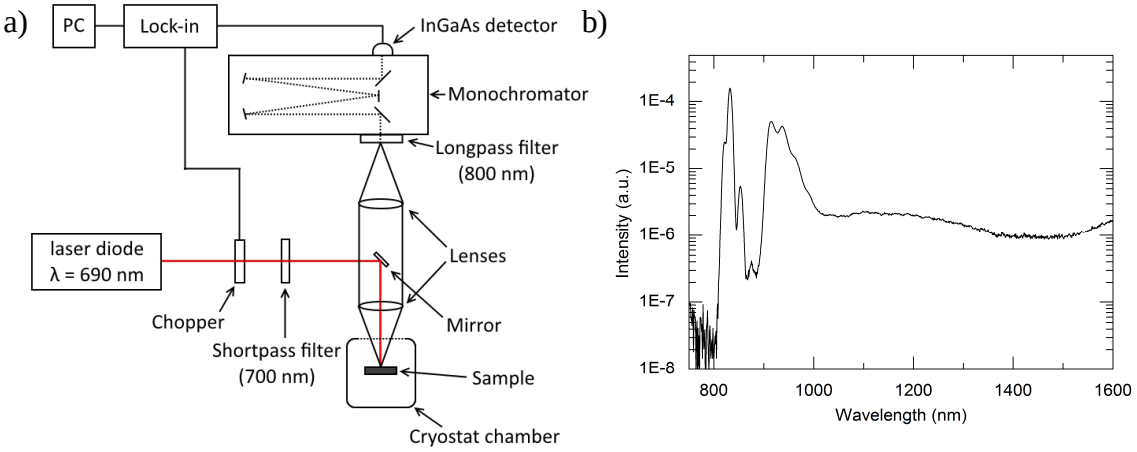

Figure 3.9 a) Schematic of the LT-PL measurement system used in this work. b) LT-PL measurement of a SI-GaAs substrate performed at a temperature of 20 K.

The peaks found in Figure 3.9b at ~915 nm, which deviate from the expected GaAs emission at ~830 nm, are ascribed to Cu acceptor levels in GaAs. This is based on the work of Queisser et al. [52], where the PL transition energies of Cu-doped GaAs are reported. A comparison between Queisser et al.'s values and the measured spectra is shown in Figure 3.10. There is excellent agreement with the peak positions and longitudinal optical (LO) phonon assisted transitions are visible as well. The LO-phonon energies inferred from the graph correspond to the well-known value of 36 meV for GaAs.

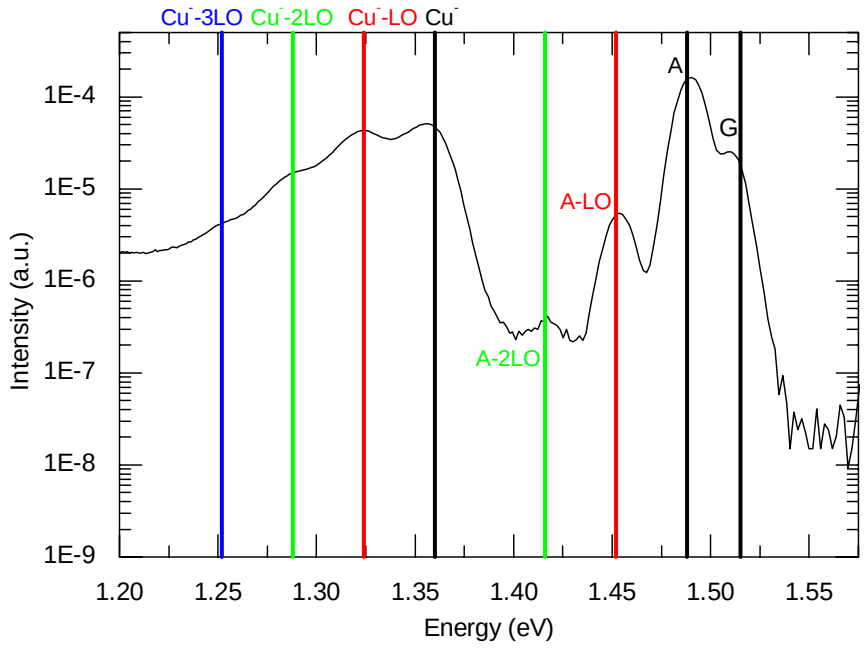

Figure 3.10 LT-PL spectra of an SI-GaAs substrate with individual peaks presented by dashed lines using data from reference [52]. The labels refer to band edge, shallow acceptor (carbon or silicon) and Cu acceptor related transitions for G, A and Cu^-, respectively. The LO-phonon assisted transitions are denoted with the number of LO-phonons excited in the transition.

3.2.3 Scanning electron microscopy

Scanning electron microscopy (SEM) allows for high resolution and high magnification imaging of surfaces. The imaging is done by rastering a focused beam of electrons across the surface while detecting signals that change in response to the electron bombardment. Typically, SEM is used for measuring surface topology/morphology or surface chemical composition. For conventional SEM imaging, the sample must be electrically conductive or be coated with a conductive material to prevent electrostatic build-up at the surface. Subsequently, for semiconductor research the imaging is swift as sample preparation is not required and non-destructive as the incident beam energies aren't sufficient for structural damage.

The SEM imaging in this work is done by two different detectors, which yield different information about the surface. Insight into the surface topology is provided by a secondary electron (SE) detector. This detection mode provides high depth-of-field images of the surface with three-dimensional appearance. The SEs are ejected from the first few atomic layers of the specimen by inelastic scattering interactions with the incident beam (primary) electrons. These electrons have low kinetic energy (below 100 eV) in comparison to the incident beam electrons (typically in the order of 100 to 10 000 eV). The

topographical contrast is achieved due to the low escape depth of the SEs and the angular dependence of the SE yield between the incident beam and the surface. [53]

A backscattered electron (BSE) detector is used for compositional imaging. The BSEs are primary electrons that have elastically scattered from the surface. These electrons can be distinguished from the SEs by their kinetic energy, as they have approximately the same kinetic energy as the primary electrons (E_0 in Figure 3.11a). The compositional contrast is achieved due to the elastic scattering probability being proportional to the atomic number. [53]

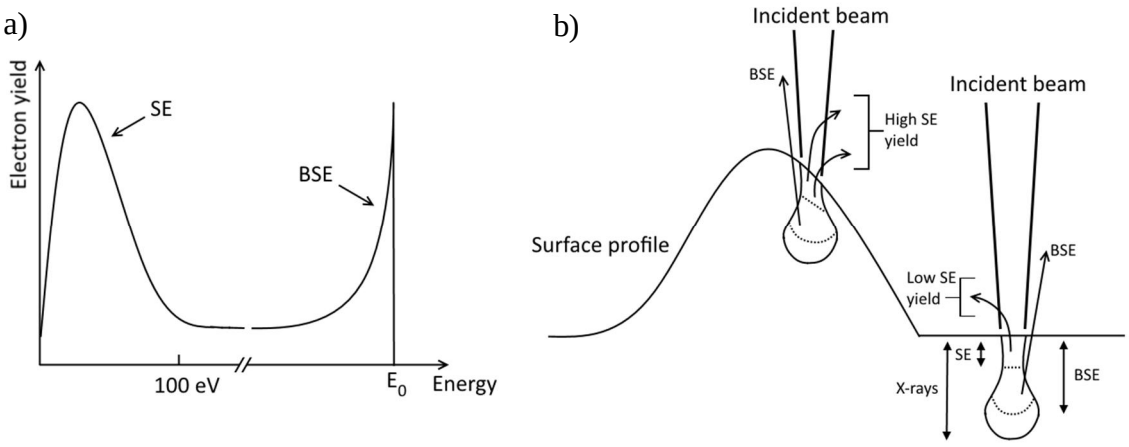

Figure 3.11 a) Distribution of emitted electrons from a specimen under SEM electron bombardment as a function of their kinetic energy. b) Schematic of relative escape depths of X-rays, BSEs and SEs due to the incident electron beam with an illustration on how topographical contrast is achieved by SE imaging.

The SEM imaging in this work was done with a Zeiss Ultra-55 microscope. It is fitted with a field emission electron beam source, which provides a much narrower probing beam than typical thermionic emitters resulting in an improved spatial resolution up to ~1 nm. The primary beam electrons can be accelerated with voltages ranging from 0.1 to 30 kV and are conditioned into a focused beam by magnetic lenses. The SE detector is mounted into the magnetic lens column (referred to as an In-lens detector) to achieve higher contrast and better resolution. The BSE detector is a more traditional out-lens detector fitted a filtering grid.

3.2.4 Atomic force microscopy

Atomic force microscopy (AFM) is a method by which surface topography can be measured with sub-nanometer resolution. In contrast to SEM, AFM provides accurate spatial information perpendicularly to the surface. Furthermore, no sample preparation is needed and the method is generally thought of as non-destructive for solid surfaces, making it ideal for semiconductor research. However, AFM is considerably slower than SEM imaging due to the mechanical nature of probing the surface.

The operating principle of AFM is based on probing the sample surface by an atomically sharp tip and detecting the interactive forces between the surface and the tip. The magnitude of the interactive forces and whether the sum of these forces is attractive or repulsive is determined by the tip-to-surface distance. When the tip-to-surface distance is in the order of multiple nanometers, attractive forces, such as van der Waals, electrostatic and magnetic forces, dominate. When reducing the tip-to-surface distance below a nanometer, short range Coulomb interaction overcomes the attractive forces and an overall repulsive force dominates. The forces are typically detected by the deflection of the cantilever on which the tip is mounted to. For conventional AFM systems, this is done by tracking the reflection angle of laser light off the top of the flat cantilever head with a segmented photodiode. The topographical information is achieved by raster-scanning across the surface with the tip while holding some parameter constant. For example, the cantilever can be held at constant height during the scan and the sample surface profile can be deduced from the amount of deflection of the cantilever. Based on what parameter is held constant during the scan, AFM is divided into three imaging modes: contact, non-contact and tapping. The measurements in this work were performed using the tapping mode. [54]

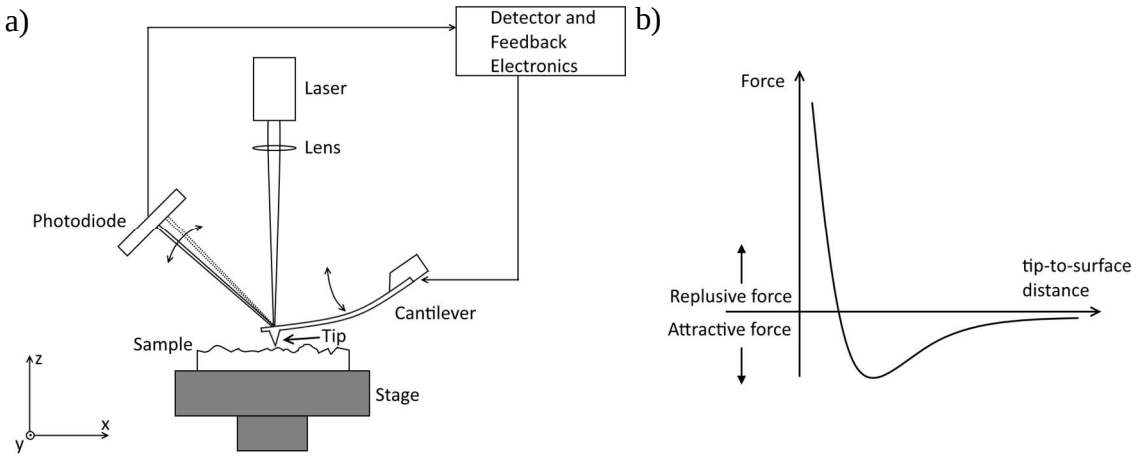

Figure 3.12 a) Schematic of an AFM system. b) The tip-surface force as a function of the tip-to-surface distance.

The tapping mode (also referred to as amplitude modulation AFM) is a dynamic operation mode of the AFM where the cantilever is deliberately vibrated during the measurement. The vibration is driven by a piezo element mounted in the cantilever holder and the vibration frequency is fixed near a mechanical resonance frequency of the cantilever. As the vibrating tip is brought closer to the surface, the resonance frequency of the cantilever shifts due to the change in external force induced by the tip-surface interaction. This, in turn, causes a shift in vibration amplitude at the fixed drive frequency (see Figure 3.13), which is chosen to be near the resonance to maximize this shift. The amount of amplitude shift therefore reflects the changes in tip-to-surface distance. Furthermore, adjusting the tip-to-surface distance over the raster-scan so that the vibration

amplitude is constant, allows for the accurate determination of the surface topography. [54]

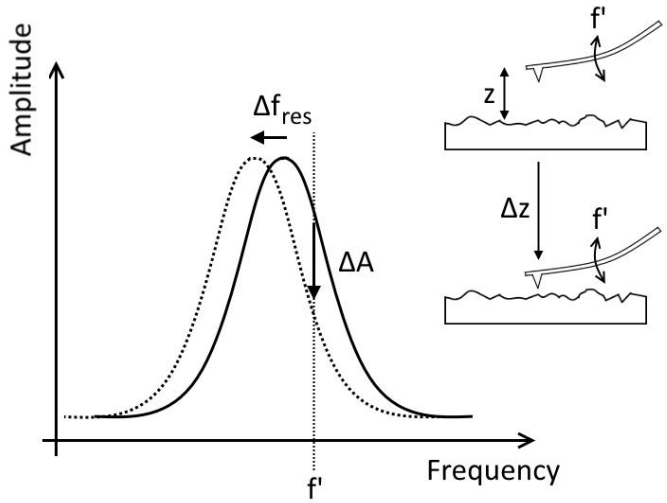

Figure 3.13 Illustration of the shift in resonance frequency Δf_{res}, resulting in an amplitude shift ΔA, as the tip-to-surface distance z is adjusted. At the drive frequency f' the amplitude shift is maximized.

The AFM imaging in this work was done with a Veeco Dimension D3100 instrument together with the Nanoscope IV control unit. The measurements and some of the image analysis were performed using the Veeco V613r1 software. Further analysis on the data was done using Matlab 2014a/2015a software.

4. RESULTS

In this chapter, the results of this work are presented and discussed. An in-depth analysis on the growth parameters in stationary growth is performed. This is achieved by the stationary growth of structures whose properties are known to be controlled by a specific growth parameter. The growth parameter spatial variation is then deduced by the measurement of these properties across the grown wafers. Due to the scope of this work, only the growth parameters relevant to GaAsBi growth are analyzed, namely As, Bi and Ga fluxes and the growth temperature.

After the spatial variability of the growth parameters are known, the stationary growth of GaAsBi structures, namely bulk layers and quantum wells (QW), is performed. These structures are then characterized to ascertain information on how the growth parameters influence the properties of these GaAsBi structures. A focus of this work is to provide a general overview of growth parameter influence on GaAsBi material properties with a relatively high Bi composition. It should be noted that the results presented here cannot be generalized to different Bi compositions or growth conditions. Additionally, this work offers a methodology in MBE research for novel materials that reduces the required amount of growths while improving material reproducibility.

4.1 Determination of growth parameters in stationary growth

4.1.1 Gallium flux

The determination of spatial variation of the Ga flux is simple because the Ga flux controls the GaAs layer thickness independently of other growth parameters at standard GaAs growth conditions. To determine the Ga flux distribution across the wafer, it is therefore only required to grow a standard GaAs layer and measure its thickness across the wafer. However, to determine the GaAs layer thickness a marker layer is required, as the structure of the buffer layer and the GaAs layer are identical. For this work, an AlAs layer was used as a marker layer and was placed between the buffer layer and the GaAs layer of interest, forming a basic AlAs/GaAs heterostructure. The AlAs lattice mismatch with respect to GaAs is small enough to grow relaxation-free interfaces but large enough to enable HRXRD analysis, with which the grown layer thicknesses could be determined.

The nominal AlAs/GaAs heterostructure layer thicknesses were chosen to maximize the amount of HRXRD intensity fringes while keeping the total thickness of the structure

below 0.5 µm to have manageable growth times with the ~0.7 and ~0.5 µm/h growth rates used for the AlAs and GaAs layers, respectively. Specifically, nominal thicknesses of 75 nm and 250 nm (i.e. a 3:10 ratio) were chosen for the AlAs and GaAs layers, respectively. Figure 4.1 shows a HRXRD measurement and simulation from the center of the wafer of this grown structure.

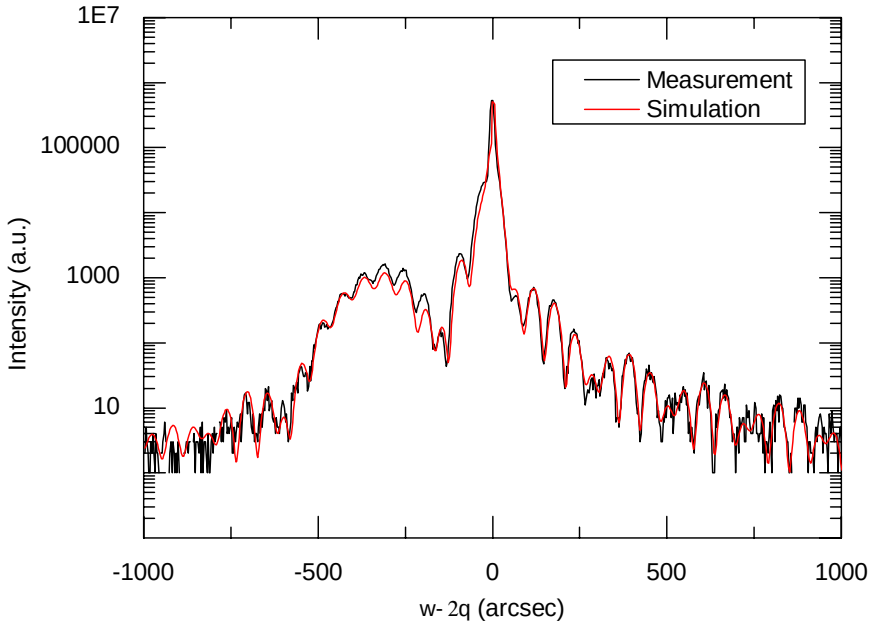

Figure 4.1 HRXRD measurement and simulation of the AlAs/GaAs heterostructure from the center of the wafer.

The AlAs marker layer was grown with rotation to produce a uniform layer thickness across the wafer, which was confirmed by the HRXRD analysis. The rationale for this was to improve the sensitivity of the HRXRD analysis, so that any change in the HRXRD spectrum would only be reflected by the change in the topmost GaAs layer thickness. The rotation speed and the growth temperature for the AlAs layer was the same as that of the buffer layer. The As flux was adjusted to be slightly higher for the growth of the AlAs layer to accommodate the higher growth rate with respect to the GaAs layer. After the marker layer was grown, the manipulator rotation was stopped and the GaAs growth was started with the same growth parameters as the buffer layer (see chapter 3.1.1).

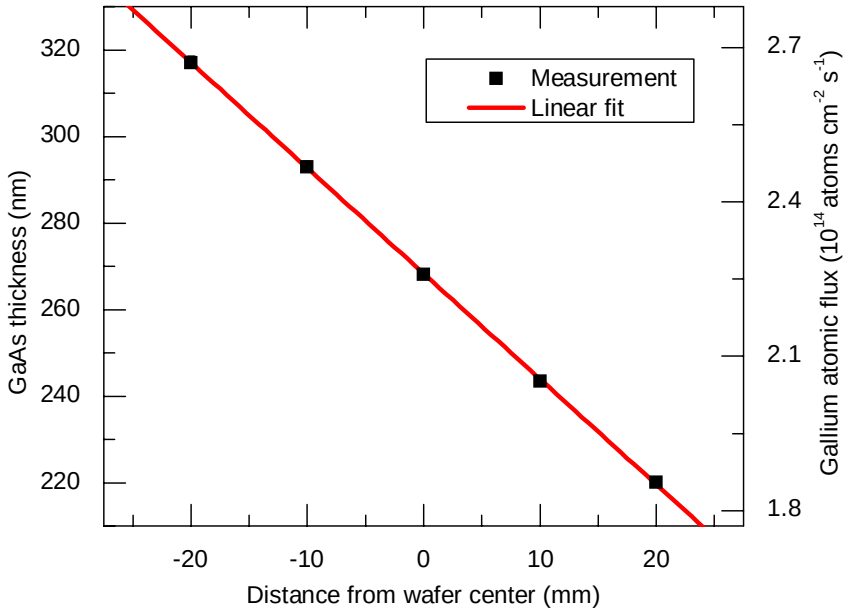

Figure 4.2 GaAs film thickness across the wafer determined by HRXRD simulation. The Ga fluxes corresponding to the GaAs film thicknesses are depicted on the right hand side axis.

The grown sample was then measured by HRXRD over multiple locations across the wafer. Based on the HRXRD analysis, the GaAs thickness was found to vary significantly only in one direction. The GaAs thickness along this axis is shown in Figure 4.2. If the flux distribution is assumed to be conventional, i.e. the flux density is proportional to the cosine of the angle with respect to the cell orifice normal, these results imply that the focal point (maximum flux density position) is offset significantly from the wafer center. The Ga flux was calculated from the GaAs thickness by a simple amount of substance calculation based on the thickness, growth time and density of the GaAs layer. The Ga flux relative decrease was ~0.9 %/mm across the wafer along the gradient maximum axis.

4.1.2 Bismuth flux

Due to Bi incorporation being sensitive to practically all growth parameters, the Bi flux is hard to determine spatially by the growth of GaAsBi structures. Therefore, a simple pure Bi deposition sample was grown without rotation to determine the Bi flux distribution across the wafer. The deposition was conducted at a low growth temperature of ~220 °C to ensure that all of the incident Bi atoms stick to the surface. The deposited Bi atoms nucleate on the surface forming metallic Bi droplets. The total amount of Bi atoms in the droplets at particular location on the wafer would then be representative of the incident Bi flux at the corresponding location. A similar methodology for calibrating the Bi flux has been used in reference [24].

The estimation of the amount of Bi in a particular area of the wafer required the knowledge of the Bi droplet geometry. Therefore, a simple geometric model was formulated based on AFM measurements from a Bi deposition sample. Two examples of these AFM measurements are shown in Figure 4.3. From these measurements, the base areas and volumes of the Bi droplets would be acquired. A model would be then fitted between these two quantities, shown in Figure 4.4.

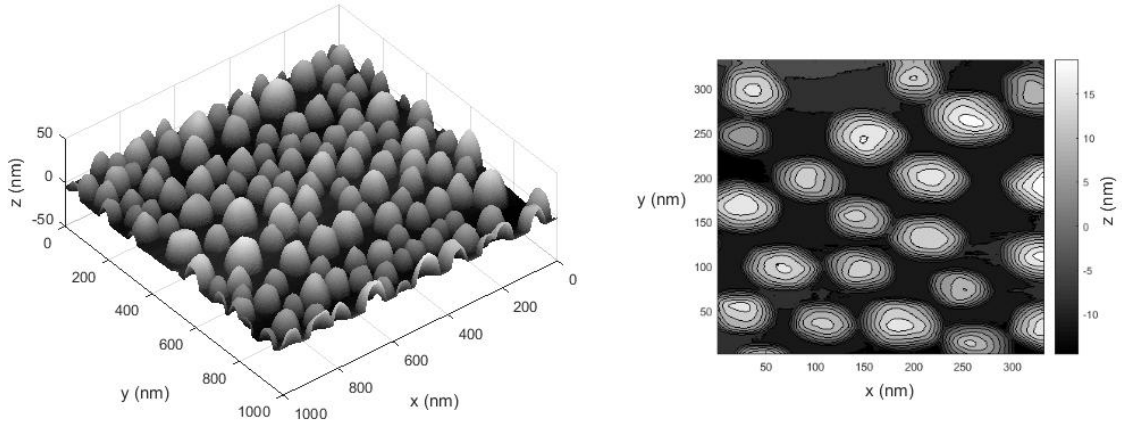

Figure 4.3 AFM measurements of a surface covered with pure Bi droplets. On the left, a three dimensional overview of the surface and, on the right, a two dimensional contour plot of the Bi droplets, illustrating their non-spherical nature.

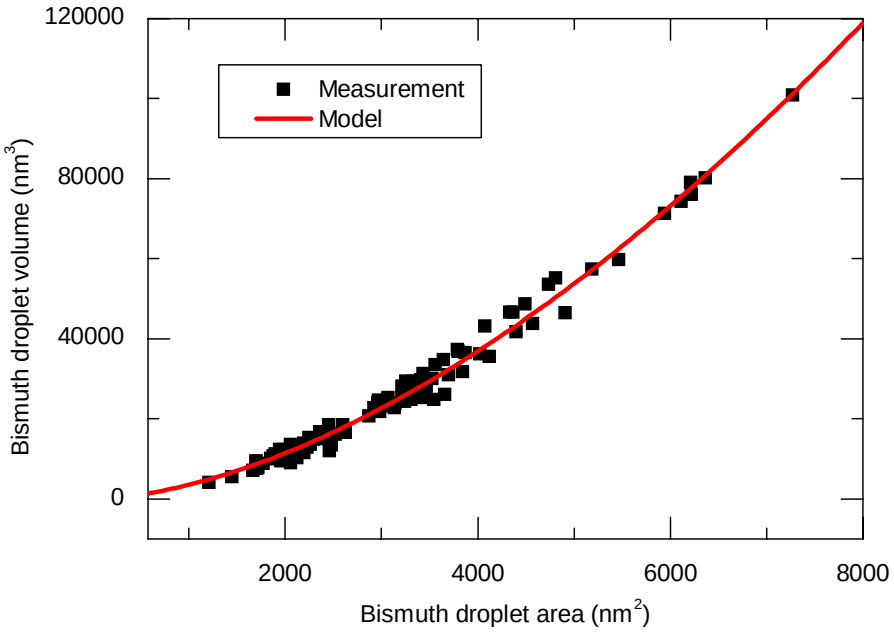

Figure 4.4 The dependency of Bi droplet volumes with respect to their base area.

Formulation of this model enabled the calculation of the amount of Bi from SEM images, which would result in a much faster analysis across the wafer as SEM imaging is a faster process compared to AFM imaging. Due to the compositional contrast of the BSE detector SEM images, the Bi droplets can be clearly differentiated from the background

GaAs. The determination of the droplet areas is therefore simple with any image analysis software.

The Bi deposition sample was measured by SEM from multiple locations across the sample. No major variation in the droplet coverage was observed in any direction. Therefore, the amount of deposited Bi was only calculated accurately along the same axis as the maximum Ga flux gradient. The axis corresponding to Figure 4.2 was measured by SEM in 5 mm steps. The Bi droplet areas were determined from BSE detector images by ImageJ-software. An example of the result of this analysis is shown in Figure 4.5b.

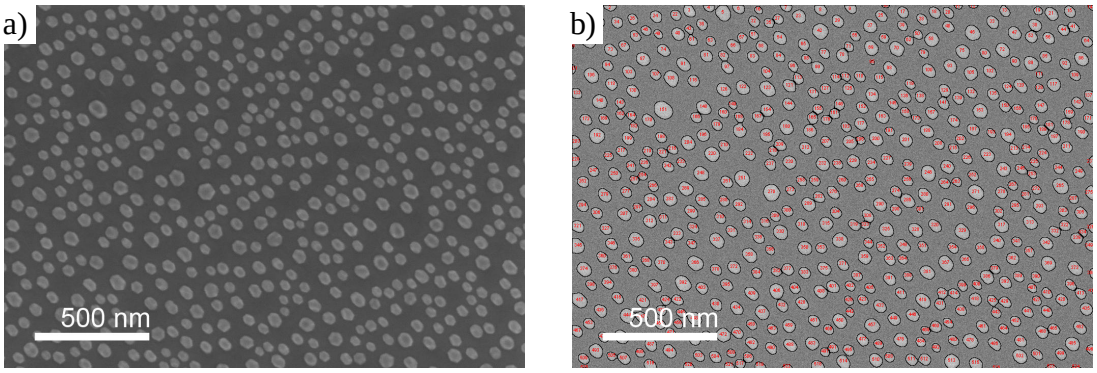

Figure 4.5 a) A SE detector SEM image of the Bi droplets. b) A BSE detector SEM image from the same area overlaid with the determined droplet areas (outlined in black and numbered in red).

The total volume of Bi in a particular imaging area was calculated by the summation of the individual droplet volumes, which were in turn calculated from the droplet areas using the model in Figure 4.4. The amount of Bi atoms corresponding to this volume was calculated from the known atomic weight and density of (rhombohedral) Bi. By relating the amount of Bi atoms to the imaging area and the deposition time, the incident Bi flux was calculated at each measurement location. The left hand side of Figure 4.6 shows the calculated Bi flux across the wafer.

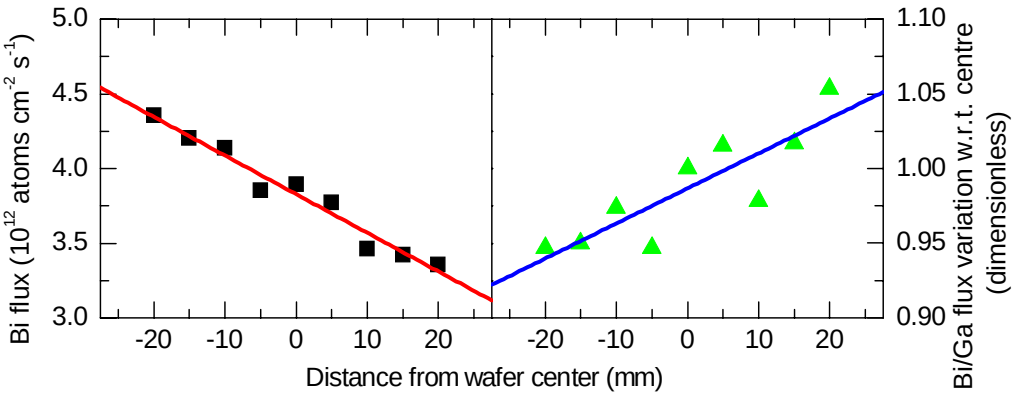

Figure 4.6 Left: The Bi flux across the same axis as Figure 4.2 with a linear fit. Right: The ratio of the Bi and Ga fluxes relative to the center of the wafer.

The right hand side of Figure 4.6 shows the relative Bi/Ga flux ratio normalized to the center of the wafer. Due to the Bi flux decreasing slower than the Ga flux across the wafer, the Bi/Ga ratio increases slightly going towards the positive side of the axis. As mentioned previously in chapter 2.3, the Bi incorporation in GaAs increases approximately linearly when increasing the Bi/Ga flux ratio at stoichiometric As/Ga flux ratios. Therefore, the relative Bi incorporation rate across the wafer can be approximated from Figure 4.6, assuming that the As/Ga flux ratio across the wafer is constant and stoichiometric. For example, for a 5 % target incorporation of Bi at the center of the wafer, the outermost measurement locations of the 2” wafer (specifically at ±20 mm from the center) would have 4.75 % and 5.25 % of Bi for the negative and positive sides of the axis, respectively. For this work, this variation will be considered to be negligible, due to the dominating effect of the As/Ga flux ratio on the Bi incorporation rate, which will be shown in chapter 4.2.1.

4.1.3 Arsenic flux

The volatile nature of the As species hinders accurate analysis of the As flux. Specifically, an analysis method similar to the determination of the Bi or Ga flux spatial variation is likely not possible, as As has a low sticking coefficient even at growth temperatures near room temperature (resulting in an As overpressure) and incorporates to the GaAs surface as an amorphous As layer. This is evident from several reports on the growth of pure As layers [55, 56], which are often used for passivating surfaces. Therefore, a novel method was developed for the determination of As flux, based on the growth and analysis of a LT-GaAs layer grown under the As-limited growth regime (i.e. As/Ga flux ratio below unity). This method is presented and reviewed in detail in my Bachelor’s thesis [57] and therefore only a cursory description of the method is outlined here.

As mentioned above, the method relies on the analysis of a LT-GaAs layer grown under As-limited conditions. The rationale for the growth parameters is to inhibit any desorp-

tion of the incident Ga and As during growth and to ensure that all of the incident As is incorporated into the layer. A growth temperature of ~220 °C is used to make any desorption negligible and the As-limited growth regime is used to enable a practically unity sticking coefficient for the As species, due to the excess amounts of available group V sites on the growth surface. The thickness of such an LT-GaAs layer is therefore proportional to the As provided. However, the thickness is hard to distinguish due to similarity of the underlying GaAs substrate to the LT-GaAs layer. A marker layer, such as in chapter 4.1.1, can be used to circumvent this issue, for example. A more elegant solution, however, is to determine the amount of excess Ga that accumulates as metallic Ga droplets on the LT-GaAs surface, due to the As-limited conditions used. The incident As flux can be then calculated based on the amount of Ga on the surface, namely the As flux is inversely proportional to the amount of surface Ga. The amount of Ga in the droplets can be calculated using the same methodology as for the calculation of Bi atoms in chapter 4.1.2. Again, for a more comprehensive examination of this method, the reader is referred to reference [57].

Two samples (referred to as samples #1 and #2) were grown using the aforementioned growth parameters. Specifically, the As/Ga flux ratios for the samples were estimated from ion-gauge measurements to be nominally ~0.7 and ~0.55 for samples #1 and #2, respectively. The stationary growth mode resulted in an As/Ga flux ratio gradient across the wafer, from which the As flux was calculated using the method described above. The gradient in the As/Ga flux ratio was large enough to form two separate surface phases: one where the surface was covered in Ga droplets (As-limited regime) and one where the surface was smooth (As-rich regime). The relative areas of these phases are depicted in Figure 4.7. The interface between these two regimes was observed to be well-defined and linear with an optical microscope. Additionally, based on observations of the growth orientation with respect to the source material cells (see Figure 4.7), the direction of the As/Ga gradient was found to be reproducible. The linear interface was perpendicular to the Ga flux gradient axis, which suggested that the As flux variation would be negligible, as the position of the interface is sensitive to the As/Ga flux ratio and considering that the Ga flux gradient is the same along the length of the interface.

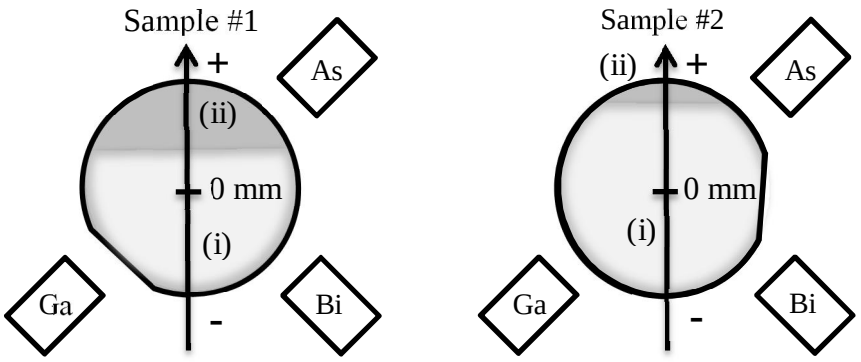

Figure 4.7 Schematic diagram of the two surface phases: (i) an area with As-limited conditions forming droplets and (ii) an area with As-rich conditions with a smooth surface. The arrow represents the Ga flux gradient axis and the labelled boxes represent the cell orientation with respect to the wafer during growth.

The samples were measured by SEM along the Ga flux gradient axis in 5 mm intervals and, from the BSE detector images, the As flux was calculated based on the amount of Ga on the surface. A rough illustration of how the total amount of Ga on the surface behaves is depicted in Figure 4.8, where the droplet sizes rapidly decrease when going towards the As-rich side of the wafer.

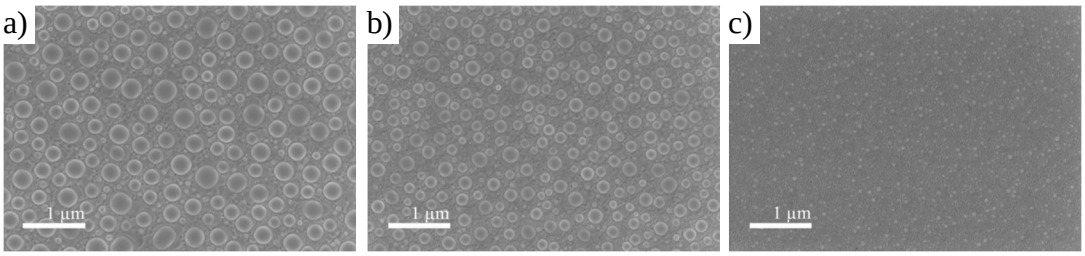

Figure 4.8 SE detector images of sample #1 along the Ga flux gradient axis at a) -15 mm, b) -5 mm and c) +5 mm.

The calculated As flux and As/Ga flux ratio gradients across the wafers are shown in Figure 4.9. The respective Ga flux values used in calculating the As/Ga flux ratio in the right hand side of Figure 4.9 were calculated based on the previously determined Ga flux gradient (from Figure 4.2) and its proportionality to the individual BEP values used in the growths. Despite the different absolute As flux values used, the As flux distribution across the wafers are similar for both of the samples, again demonstrating good reproducibility. Specifically, the As flux has an average slope of -4×10^{11} atoms $cm^{-2}s^{-1}$/mm, whereas the Ga flux slope is an order of magnitude higher at -3×10^{12} atoms $cm^{-2}s^{-1}$/mm, indicating that the Ga flux is a dominating factor in the resulting As/Ga gradient.

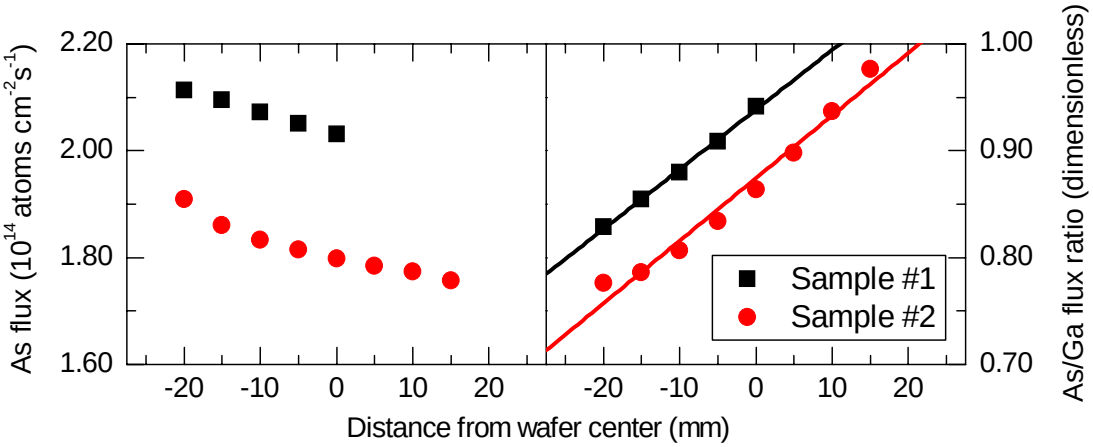

Figure 4.9 The calculated As flux and As/Ga flux ratio variation across the same axis in Figure 4.2.

4.1.4 Growth temperature

To measure the growth temperature variation across the wafers during stationary growth, a knowledge of point defect incorporation rates in LT-GaAs with respect to the As/Ga flux ratio and growth temperature was applied. As mentioned in chapter 2.2, when increasing the As/Ga flux ratio to a sufficiently high value, the point defect incorporation is saturated or, in other words, independent of As and Ga fluxes. However, when increasing the growth temperature the saturated concentration of the point defects decreases linearly. Therefore, a change in the growth temperature across the wafer would result in a change in the concentration of the point defects.

For a comprehensive analysis of the growth temperature variation in stationary growth, several LT-GaAs layers were grown without rotation at different temperatures using the same As/Ga flux ratio of ~2.7. The concentration of point defects was estimated from the compressive strain that the point defects induce, which scales linearly with the concentration [19]. The strain, here simply represented as a mismatch value (see Figure 3.6), was determined by HRXRD measurements across the Ga flux gradient axis. The results of these measurements are shown in left hand side of Figure 4.10.

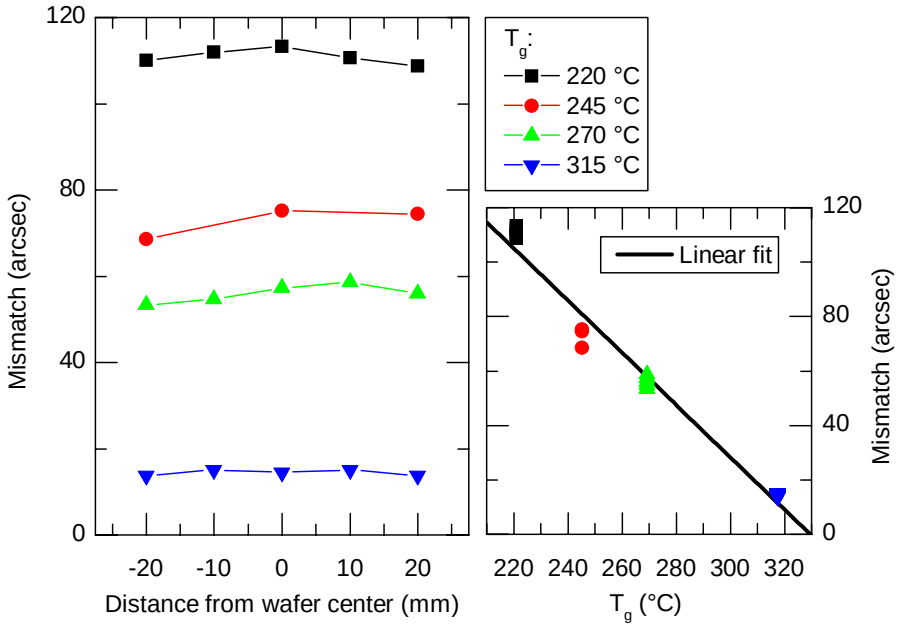

Figure 4.10 Left: The mismatch variation across the Ga flux gradient axis measured by HRXRD. Right: The average of the mismatch values at each temperature fitted with a linear fit.

From the left hand side of Figure 4.10, the variation of the mismatch was observed to be relatively constant. However, the sensitivity of the mismatch shift with respect to the temperature was not known and could not be determined accurately solely based on literature, due to the various differences in the growth parameters used. Therefore, a linear relationship was determined between mismatch (i.e. point defect concentration) and growth temperature, shown in the right hand side of Figure 4.10. The sensitivity of the mismatch shift from Figure 4.10 is approximately -1 arcsec/°C.

For a more in-depth spatial analysis, a wafer grown at the lowest temperature was measured along multiple different axes across the wafer. The mismatch values across the wafer are presented in Figure 4.11.

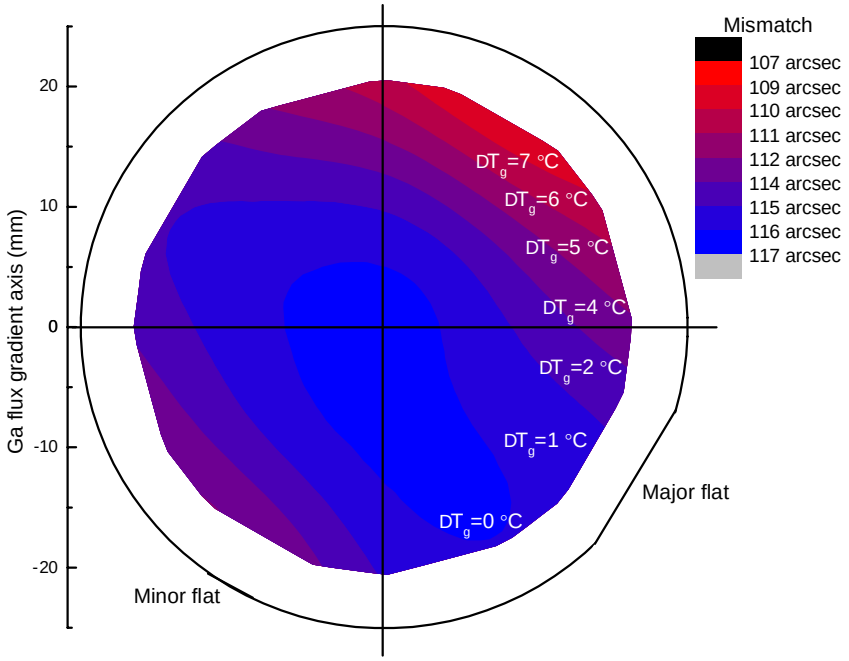

Figure 4.11 Temperature variation across the wafer determined from multiple measurements along different axis. The contour labels show the relative temperature difference with respect to the wafer center, which is calculated based on the linear relationship in Figure 4.10.

As seen from Figure 4.11, the variation in the mismatch, and therefore growth temperature, across the wafer is low. Specifically, a maximum temperature difference of ~7 °C is estimated by this method, which is within the accuracy that the growth temperature can be controlled [58]. Therefore, for this work the temperature variation across the wafer during growth is assumed to be negligible.

4.2 Characterization of GaAsBi bulk layers

The characterization of GaAsBi bulk layers in this work is performed with respect to their structural and photoluminescence properties. These properties are evaluated in the following chapters by HRXRD, SEM and PL measurements. A focus of this study is in relatively high Bi-fraction materials, namely ~5 %-Bi. Generally speaking, bulk GaAsBi samples with similar Bi-fractions in literature either show severe degradation of the HRXRD spectra or the spectra is not shown. Additionally, the layers are often well below 100 nm, implying that compositional uniformity for truly bulk layers is difficult to achieve. Moreover, these high Bi content films are often grown in a Bi saturated and As-limited growth mode [17], resulting in Ga or Ga/Bi droplets. This work therefore investigates three nominally 150 nm GaAsBi layers grown at different temperatures without rotation in hope to elucidate the structural properties of these high Bi-fraction bulk materials with respect to their growth parameters.

The three samples were grown with the same nominal Bi/Ga and As/Ga flux ratios but at different growth temperatures, namely at ~220 °C, ~320 °C and ~370 °C. The nominal Bi-fraction estimate was ~4.7 % based on the Bi/Ga flux ratio measured by the ion-gauge. Similarly, the nominal As/Ga flux ratio was estimated based on ion-gauge measurements and set to the stoichiometric value. However, as the GaAsBi layer was grown without substrate rotation, an As/Ga gradient formed, which was observed to be orientated in the same direction as those of Figure 4.7, albeit with some variation in the absolute interface position between the As-limited and As-rich side on the wafer due to run-to-run variation in the absolute As flux value. The As/Ga flux gradient axis on the wafers were centered so that the stoichiometric As/Ga value would correspond to the interface where Ga droplets were no longer observed by optical microscopy or SEM.

A nominal growth rate of ~0.47 µm/h was used for all the bulk samples. This growth rate enabled the high As/Ga flux ratio requirements for the GaAs buffer layer without needing to ramp the As bulk temperature during growth, which would require long stabilization times and result in larger uncertainties in the nominal As flux. Due to the formed As/Ga gradient during stationary growth, the growth rate also varies over the wafer. At the As-limited size the bulk growth rate is controlled by the As flux whereas in the As-rich side the Ga flux controls the growth rate. For this work, the growth rate variation based on the flux distributions over the wafer are assumed to be negligible with respect to GaAsBi growth. For example, assuming that the Bi incorporation is linearly dependent on the growth rate [29] or, in other words, a unity sticking coefficient for Bi across the whole wafer, a nominal target of ~5 %-Bi at the center of the wafer would result in ~5.04 and ~4.31 %-Bi at the As-limited and the As-rich extreme locations (specifically at ±20 mm from the center) on the wafer, respectively. Again, this effect of the growth rate variation will be shown to be negligible in comparison to the effect of the As/Ga flux ratio in terms of Bi incorporation in chapter 4.2.1.

4.2.1 High resolution X-ray diffraction

The HRXRD spectra and Bi-fraction as a function of the As/Ga flux ratio of the GaAsBi bulk layer grown at the lowest growth temperature is shown in Figure 4.12. The Bi-fraction was determined by RADS for positions along the As/Ga gradient with well-defined thickness fringes and from mismatch values for samples with degraded HRXRD profiles. Specifically for the latter case, the mismatch is almost linearly dependent on the strain and therefore Bi concentration (via Vegard's law), so a linear relationship between a mismatch value and a corresponding Bi concentration was determined by RADS.

The structural quality of the GaAsBi layer is evidently highly sensitive to the As/Ga flux ratio, as seen from Figure 4.12. At below stoichiometric As/Ga values, the HRXRD profile is severely degraded showing a broad low intensity distribution, suggesting inhomogeneous layer composition and poor interfacial quality. At stoichiometric As/Ga

flux ratio values, a pronounced growth window for good structural quality GaAsBi is shown. However, when increasing the As/Ga value only slightly above stoichiometric values, the Bi concentration quickly decreases in the layer together with the onset of structural disorder.

Another important feature of Figure 4.12 is that the Bi-fraction in the below stoichiometric regime is smaller than that of the optimal growth window regime, which indicates some disagreement with Lewis' growth model, where the Bi incorporation is saturated at below stoichiometric values. This discrepancy is apparent in the other two samples as well and could be ascribed to the formation of the Ga and Ga/Bi compound droplets (see Figure 4.18a-b), which are not considered in Lewis' model. Generally speaking, the onset of droplet formation alters the total surface coverages of Bi and Ga and induces an additional (Bi consuming) term in the Bi incorporation rate equation, therefore affecting the resulting Bi-% predicted by Lewis' model. However, it should be noted that the estimated Bi-% values from the degraded HRXRD profiles can have inaccuracies, so conclusions on the validity of Lewis' model cannot be made reliably.

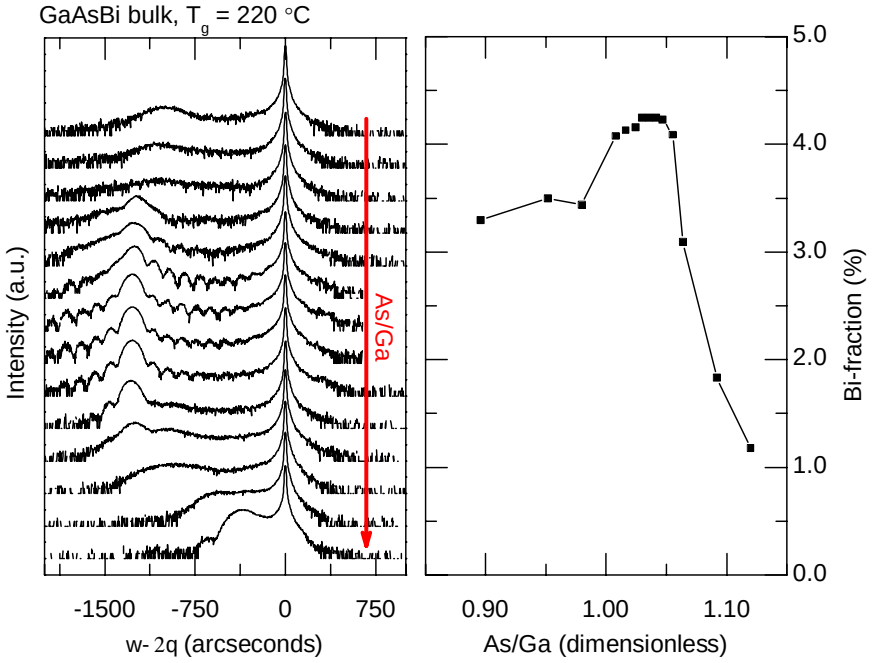

Figure 4.12 HRXRD spectra and Bi-fraction dependency on the As/Ga flux ratio of the GaAsBi layer grown at the lowest temperature.

The next sample under investigation is the GaAsBi layer grown at the intermediate temperature of ~320 °C. The change of growth temperature drastically changes the Bi incorporation as seen from Figure 4.13. At below stoichiometric As/Ga values, the HRXRD profile is again degraded showing a broad intensity distribution near the substrate peak. However, the reduction in Bi-% estimated from these profiles is much more significant when compared to the low temperature sample. This implies that the Bi evaporation or Bi incorporation into the compound droplets (possibly due to increased

surface diffusion rates) in the As-limited region is increased significantly. The near stoichiometric As/Ga ratio growth window is also much narrower (reduced to around half of the range) and has a clear decrease in the Bi-% w.r.t. increase of the As/Ga value. Furthermore, past the optimal growth window, the HRXRD spectra starts to show characteristics of a structure with two layers on top of each other with different compositions, here subsequently referred to as 'double layers'. Example simulations of these spectra are provided in Figure 4.14. The good fits indicate that the structures have sharp changes of Bi composition in the growth direction. However, the order of the high and low Bi-% layer is ambiguous solely based on HRXRD measurements and requires further study. It is noted here, that the Bi-% values presented in this work are from the simulations with least error to the measured spectra, although the respective composition values of the layers do not vary significantly between the simulations.

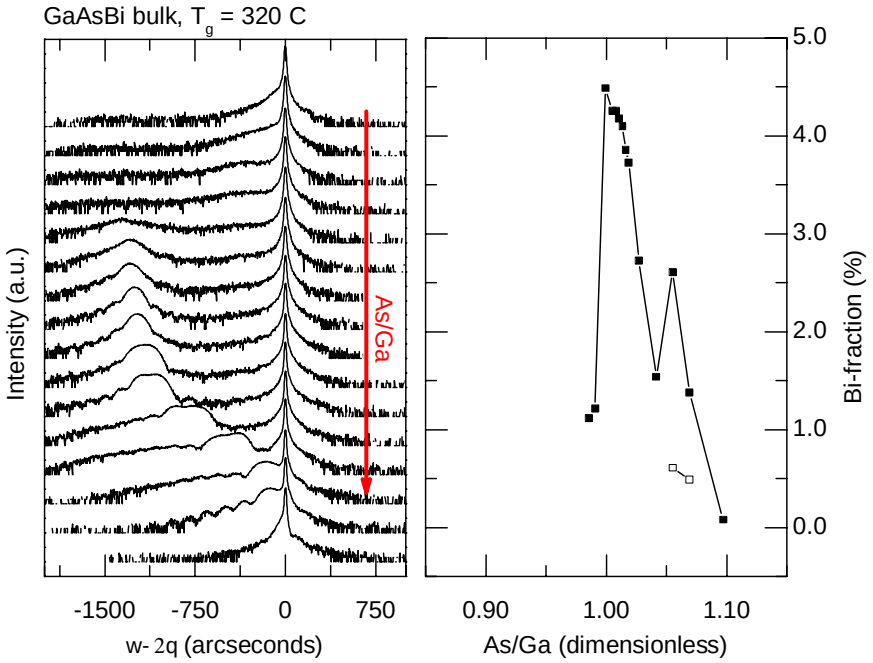

Figure 4.13 HRXRD spectra and Bi-fraction dependency on the As/Ga flux ratio of the GaAsBi layer grown at the intermediate temperature. The open symbols represent the smaller Bi-fraction of the double layered structures.

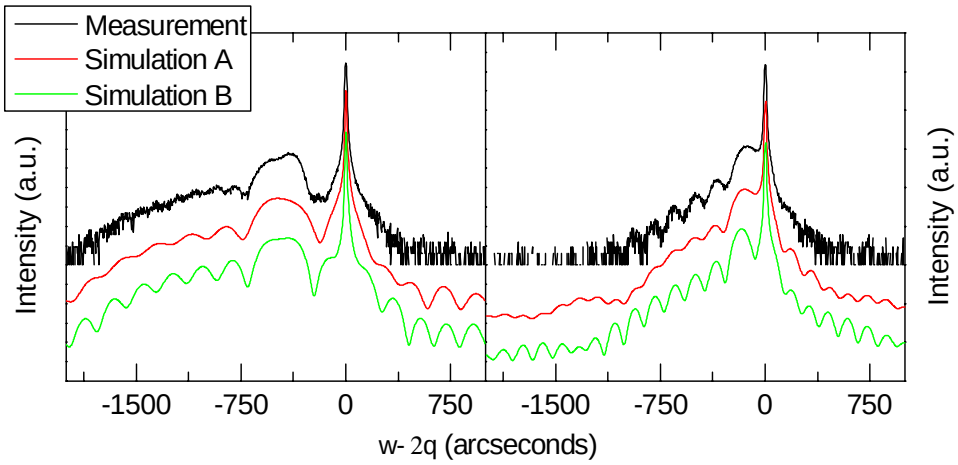

Figure 4.14 Example simulations of the double layer HRXRD profiles of the intermediate growth temperature sample. The figures show two different simulations corresponding to structure with a high Bi-% top layer and a low Bi-% bottom layer (A) and vice versa (B).

The HRXRD results for the sample grown at the highest temperature are shown in Figure 4.15. The below stoichiometric region has qualitatively the same trend as the previous samples, albeit with improved crystal quality possibly due to the high temperature used. The homogeneous growth window is even narrower than the previous samples to the extent that finding an ideal measurement of a single layer with homogeneous composition is limited by the width of the X-ray beam (~1.8 mm or the equivalent to a change of ~0.01 in the As/Ga flux ratio over the measured area). Altering the As/Ga flux ratio near the growth window affects the Bi incorporation drastically. On the one hand, reducing the As/Ga value induces double layered structures, albeit with high crystalline quality. On the other hand, increasing the As/Ga value decreases the Bi incorporation rapidly. At high As/Ga values the Bi incorporation is fully suppressed as was the case for the sample grown at the intermediate temperature.

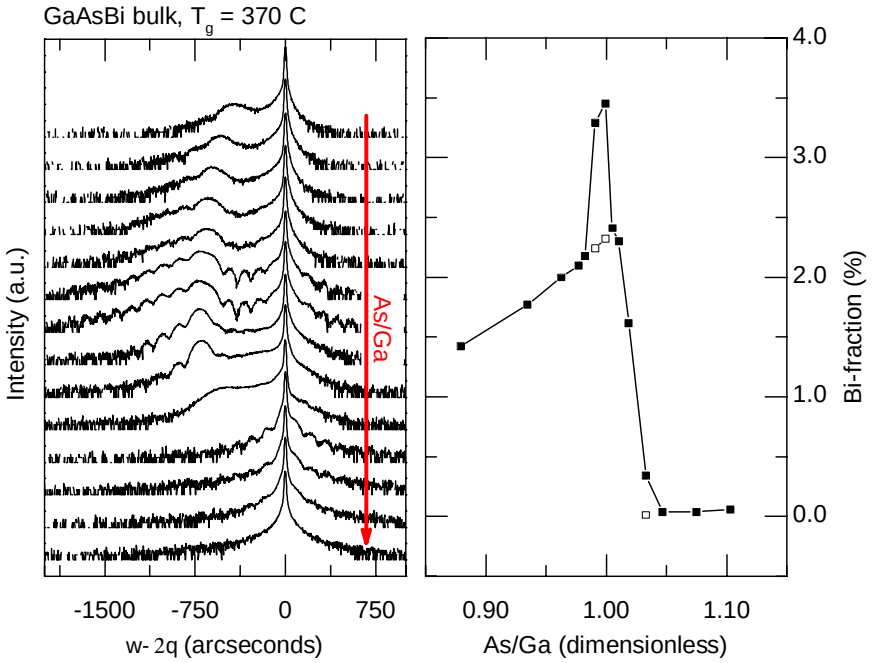

Figure 4.15 HRXRD spectra and Bi-fraction dependency on the As/Ga flux ratio of the GaAsBi layer grown at the highest temperature. The open symbols represent the smaller Bi-fraction of the double layered structures.

A compilation of the best homogeneous single layer HRXRD profiles and a comparison of the Bi-fraction dependency on the As/Ga flux ratio between all the samples are shown in Figure 4.16. The low temperature sample shows the best crystal quality single layer based on the HRXRD measurements. However, it is expected that the higher temperature grown samples also have areas with high crystalline quality single layers corresponding to the ideal near stoichiometric regime. This is due to the relatively large size of the X-ray beam with respect to the spatial As/Ga flux gradient over wafer, which averages the measurement to be a representative of a GaAsBi layer grown with a range of As/Ga values. Additionally, the double layered structures formed on the higher temperature grown samples in Figure 4.13 and Figure 4.15 show well-defined thickness fringes indicating good crystal quality. Figure 4.16 demonstrates that it is possible to grow good quality GaAsBi with a relatively high Bi-fraction over a wide range of temperatures, albeit with a highly limited growth parameter window.

The Bi-fraction dependency on the As/Ga flux ratio at different growth temperatures presented on the right hand side of Figure 4.16 reveals an important observation regarding the growth of GaAsBi: the optimal growth window moves closer to the stoichiometric As/Ga flux value when increasing the growth temperature. Any similar observations have yet not been reported in literature, possibly due to the inaccuracies in As flux control. The reason for the shift can be explained through Bi desorption. When growing at higher temperatures Bi tends to desorb more efficiently at the slightly over stoichiometric conditions, where Bi acts as a surfactant, and efficient Bi incorporation with

good crystal quality only occurs in closer to the stoichiometric regime due to higher Ga coverages.

The overall Bi incorporation efficiency is higher at lower growth temperatures, as expected from literature. Subsequently, the suppression of Bi incorporation at high As/Ga ratios is much slower at low temperatures. This can be understood through Lewis' growth model by incorporating a temperature dependent evaporation probability for the As adatoms, which results in a more gentle decrease in the Ga coverage (and therefore Bi incorporation) at above stoichiometric As/Ga ratios.

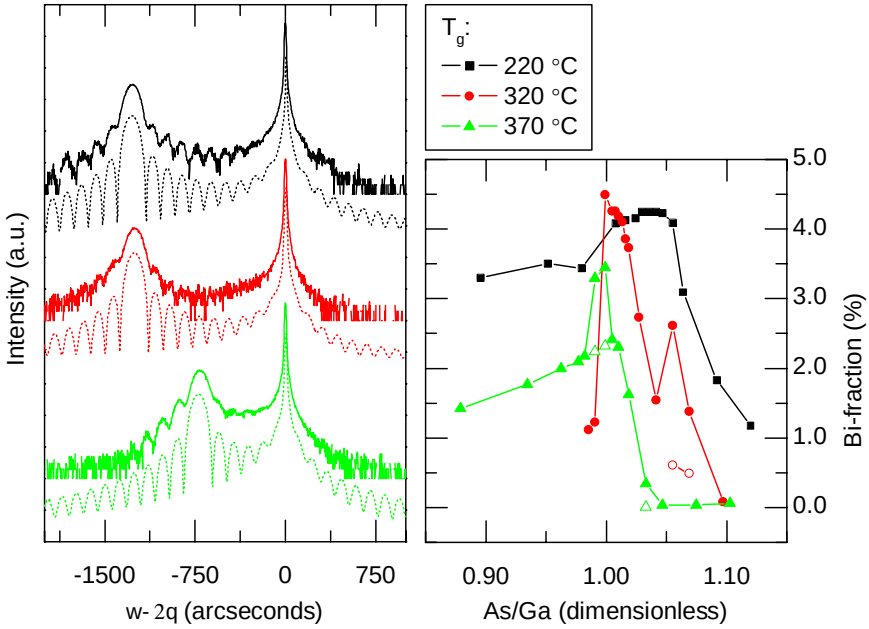

Figure 4.16 Comparison between the best single layer HRXRD spectra together with their corresponding simulations and a compilation of the Bi-fractions of the samples as a function of the As/Ga flux ratio.

Compositional non-uniformity along the growth direction has been previously reported in literature [59, 60, 61]. However, most literature shows a more continuous change in composition (e.g. an exponential decrease) rather than a more clearly defined layered structure shown here. The underlying physics behind the formation of these structures is still unknown due to the multitude of viable explanations, few of which are discussed here.

Unintentional growth parameter variation during growth is unlikely due to the double layers having a sharp interface implying a very sudden change in parameters. Moreover, if such a growth parameter change were to happen, the double layers should exist across the whole wafer (i.e. the double layers should be evident over the whole As/Ga range). Nevertheless, local variation in the As/Ga flux ratio could explain the double layers observed in the As-rich side, where both of the Bi-fractions of the double layers are comparable to adjacent Bi-fraction values on the graph. However, similar double layers are

observed for rotated samples as well [62], indicating a more fundamental growth mode change.

Another explanation for the double layers could be a change in surface reconstruction during growth. Based on the work of Masnadi-Shirazi et al. [63], two major surface reconstructions are dominant in the growth of GaAsBi, namely the (2×1) and (1×3) reconstructions. The (2×1) reconstruction enables more efficient Bi incorporation and better layer uniformity compared to the (1×3) reconstruction. However, according to the reconstruction map in reference [63], the (2×1) reconstruction should be dominant across all the growth parameters used here and would make this scenario unlikely. However, as the reconstruction map can be influenced by many factors, such as the Bi flux or the growth rate, such conclusions are tentative and would require direct observation. The change in reconstruction could, in principle, be due to exceeding some critical strain or Bi coverage value during growth and therefore induce a sudden change in the Bi incorporation rate. The reconstructions of the samples grown in this work were not measured (due to instrumentational limitations) and therefore the existence of other reconstructions or reconstruction induced changes cannot be ruled out.

Following from the previous point, a strain induced change in the Bi incorporation rate (possibly independent of the surface reconstruction) can be ruled out by considering the total strain energy involved in the surrounding areas of the double layers. As the layer grows, the strain energy, which is dependent on the composition and layer thickness, reaches some critical value and induces a permanent change in the Bi incorporation rate. However, this critical value should be exceeded in other locations over the wafer where homogeneous single layers are present and therefore is not a sufficient explanation for the formation of the double layers. Nevertheless, it should be noted that an interplay with the strain energy, growth temperature and As/Ga value could limit the double layers to the observed growth regimes.

Lastly, a change in Bi coverage or the Bi wetting layer, which controls Bi incorporation according to Lewis' growth model, during growth could also be a viable explanation. As the layer grows without fully incorporating all the available Bi or with the Bi partly segregating to the surface a growing amount of Bi accumulates on the surface. Analogously to the previous case, exceeding a critical value in the accumulated surface Bi could trigger a sudden change in the Bi incorporation rate. However, a tentative experiment conducted by growing an identical sample as in Figure 4.15 but using a pre-growth deposition of pure Bi to saturate the Bi coverage, did not suppress the formation of the double layers.

A conclusive explanation for the spontaneous formation of compositional changes in GaAsBi growth requires more research. Currently, the in-situ measurement capabilities of the MBE-reactor used in this work are insufficient to corroborate the exact cause of the double layers. Additionally, to gain more insight of the Bi incorporation properties,

more accurate and unambiguous measurement techniques are required to determine the actual Bi composition profiles across the samples. It should be emphasized, that the HRXRD method fundamentally provides an average value over the measurement area, so lateral modulation of composition in any scale below the X-ray beam dimensions cannot be detected, at least by the (004)-measurements. Microstructural composition modulation, such as reported in reference [49], is expected for (at least) the lowest growth temperature sample.

4.2.2 Reproducibility

To demonstrate reproducibility of the stationary growth method, the highest growth temperature sample was regrown. This sample was chosen as a reference based on the observed Bi incorporation sensitivity and due to the formation of double layers. The regrowth was performed during a cycle of active day-to-day MBE operation, with the growth of about 30 other samples and various flux measurements in-between the two growths. The regrowth was performed with the same nominal parameters as the original sample, with the exception of a slightly reduced growth rate (by 8 %) due to the reduced Ga flux at the chosen cell temperature caused by material consumption of the cell.

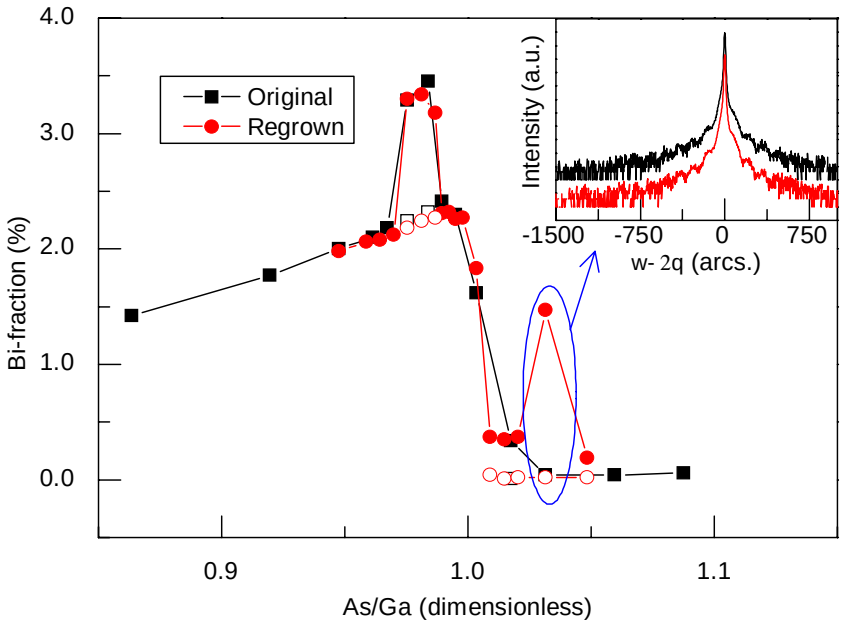

Figure 4.17 Comparison of the Bi-fractions of the original and the regrown sample as a function of the As/Ga flux ratio. The inset shows HRXRD measurements corresponding to the outlined data points.

Figure 4.17 shows a comparison between the Bi-fractions of the two samples determined by HRXRD. A good agreement in Bi-fractions is found between the samples, demonstrating the stationary growth method has excellent reproducibility over long pe-

riods of time. The PL spectra also show excellent agreement between the samples, although comparisons are omitted here.

The small discrepancies in the slightly above stoichiometric As/Ga values are ascribed to the ambiguity of the HRXRD analysis. In these areas, the low mismatch spectra can be interpreted as single layers containing a low amount of Bi or double layers containing a thin layer with relatively high amount of Bi. The inset of Figure 4.17 shows a comparison of the HRXRD spectra that correspond to the highest difference in Bi-fraction values of the main graph. The comparison shows that even though the HRXRD spectra are almost identical, different Bi-fractions can be interpreted by the HRXRD analysis. This, again, highlights the danger of relying on HRXRD alone to determine Bi composition profiles in GaAsBi samples.

The growth rate discrepancy in the reproducibility test also corroborates the previously made assumption on the effect of growth rate variability being negligible over the wafer, at least in terms of Bi incorporation and PL. The existence of double layers with the same Bi fractions (and similar thicknesses) also shows that the origin of these structures is based on a more fundamental process than random growth parameter variation.

4.2.3 Scanning electron microscopy

The structural quality of the GaAsBi layer surfaces were evaluated by taking SEM images across the As/Ga flux gradient axis. All the samples show the same general trend in surface phases: Ga/Bi compound droplets at the As-limited range, smooth surfaces at stoichiometric and slightly above range and Bi droplets at the As-rich range, with the exception that the highest temperature grown sample doesn’t have Bi droplets at the As-rich range. Therefore only the images of sample grown at the lowest temperature are presented here to illustrate that smooth GaAsBi surfaces are possible to manufacture at temperatures as low as ~220 °C.

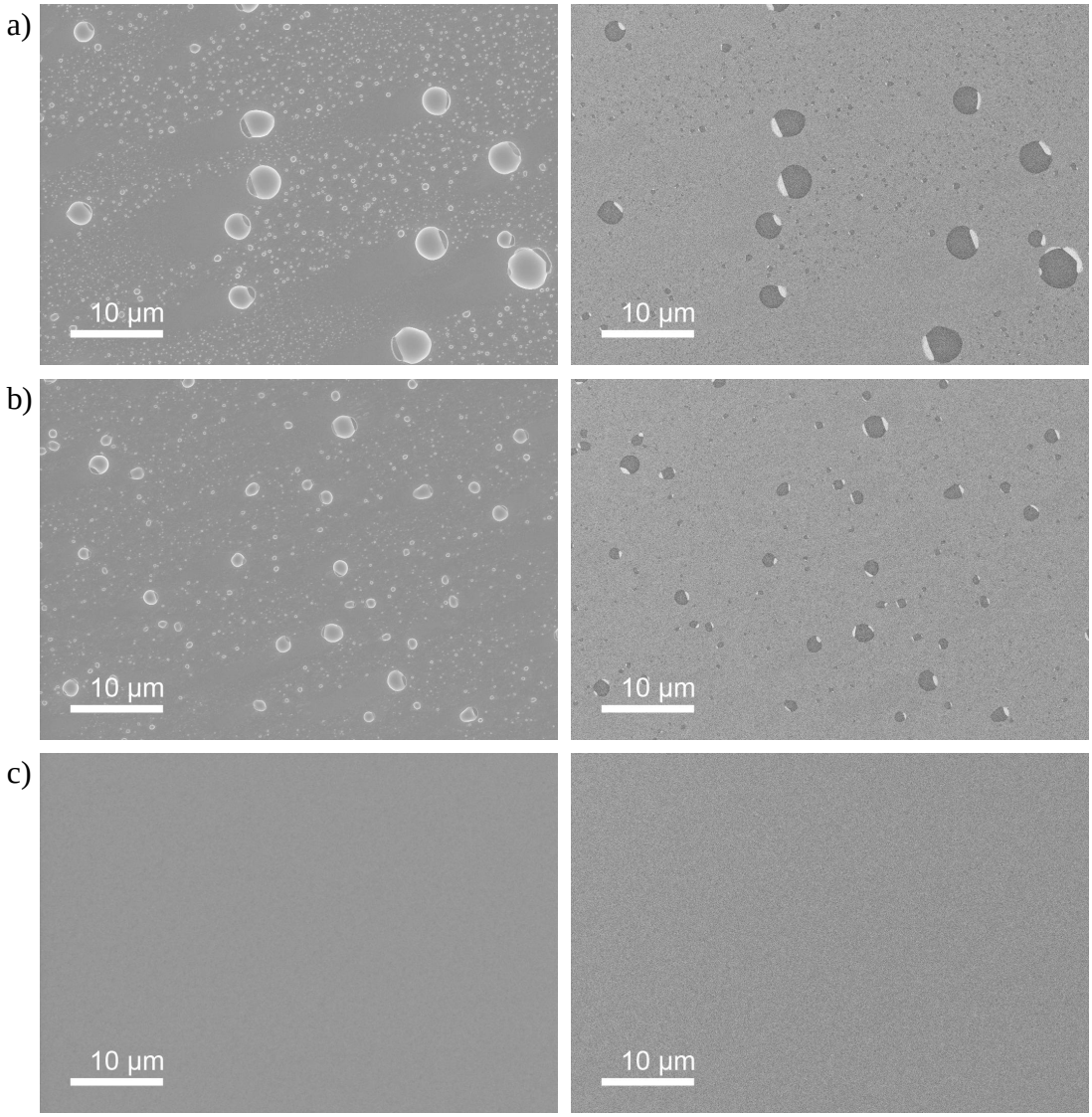

Figure 4.18 SEM SE detector (left) and BSE detector (right) images from the As-limited side along the As/Ga gradient axis. The a, b and c images are taken from locations on the wafer which correspond to As/Ga flux ratio values of 0.89, 0.97 and 1.00, respectively.

Figure 4.18 shows images of the GaAsBi layer surface grown at the As-limited regime. Ga/Bi compound droplets are observed for this regime where the droplets decrease in size with the increase of As/Ga, as expected. The compound droplets consist of a large proportion of Ga (shown as darker areas in the BSE images) together with a small accumulation of Bi (shown as bright areas connected to the dark areas in BSE images) on the side of the base Ga droplet. The orientation of the Bi component seems to favor the [110] direction. The compound droplets are divided into two sets by their size, with the larger sized droplets showing surrounding areas free of droplets. The directionality of these surrounding areas suggests that the droplets move during growth and consume the smaller droplets. In Figure 4.18a, these trails of the over 1 µm diameter droplets have a clearly defined directionality along the [110] orientation, which has been observed for pure Ga droplets on GaAs [64].

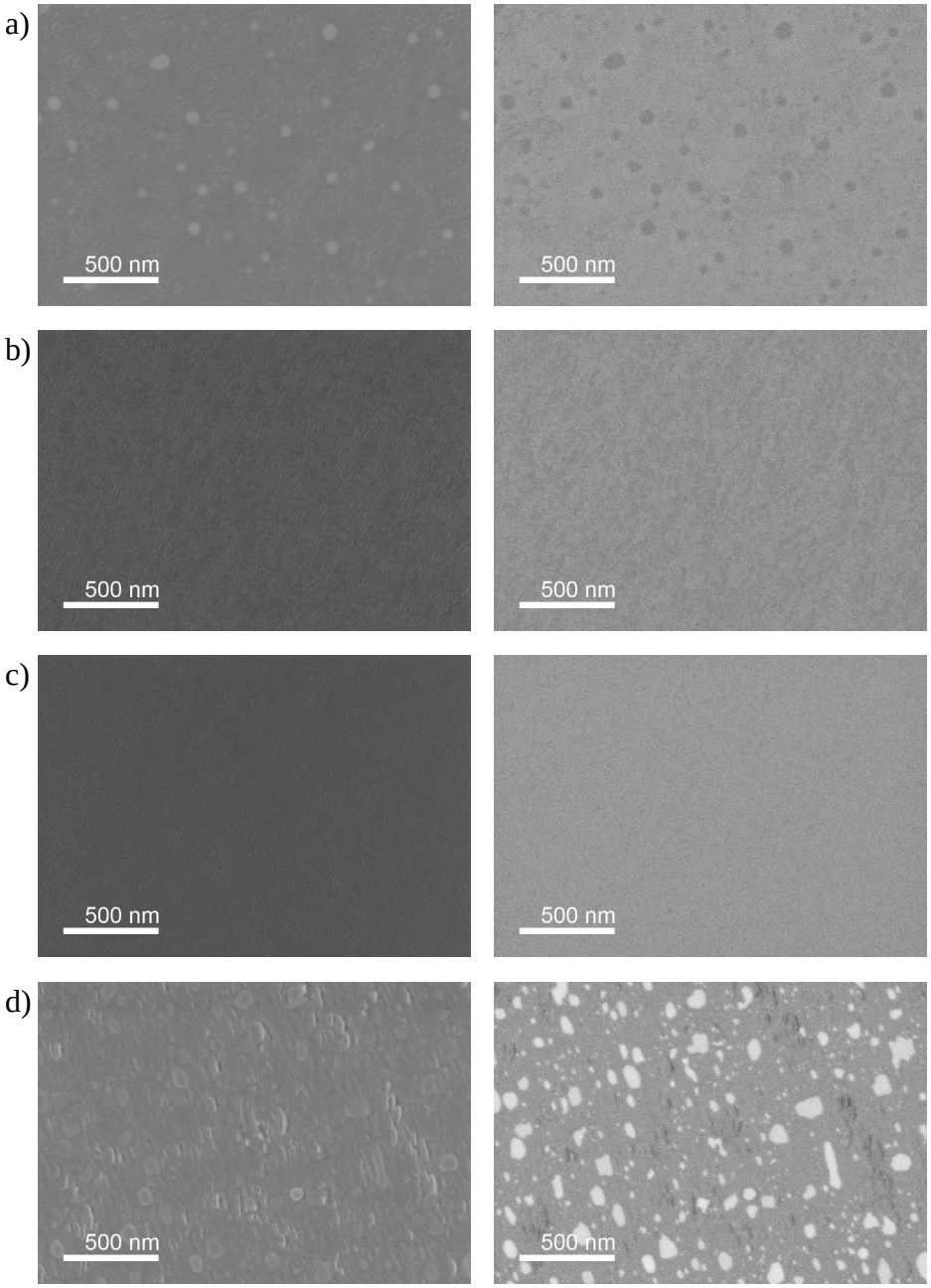

Figure 4.19 SEM SE detector (left) and BSE detector (right) images from the As-limited side along the As/Ga gradient axis. The a, b, c and d images are taken from locations on the wafer which correspond to As/Ga flux ratio values of 1.00, 1.01, 1.02 and 1.11, respectively.

A series of images taken from areas with higher As/Ga values is shown in Figure 4.19. These higher magnification images reveal that the area of Figure 4.18c that corresponds to the area of Figure 4.19a still has droplets. However, these small droplets are pure Ga, evidenced by the lack of bright areas in the BSE images, indicating an area with efficient Bi incorporation corresponding to the growth window of Figure 4.12. A slight increase in the As/Ga ratio results in areas where the BSE images seem spotty, seen in Figure 4.19b. This implies that the accumulated surface Ga in these areas is not sufficient for droplet nucleation, but the surfaces have islands with Ga rich content. Increas-

ing the As/Ga flux ratio further eliminates these islands and results in a smooth and homogeneous surface. These surfaces have nanometer scale undulations along specific crystal directions, which are typical for other good surface quality GaAsBi samples and have been reported in literature [24]. Such undulations are formed due to differences in Ga adatom surface diffusion lengths along the different crystal directions. When increasing the As/Ga flux ratio further, to such a value where the Bi incorporation efficiency is decreased, Bi starts accumulating on the surface. In Figure 4.19d, bright areas in the BSE image correspond to pure Bi droplets. These droplets are misshapen from the ideal rhombohedral droplets as seen from the Bi deposition sample (see Figure 4.5), possibly due to the very rough surfaces formed around the droplets due to the relative immobility of the Bi droplets as compared to Ga droplets. The dark areas in the Figure 4.19d ESB image are due to the topology of the surface, namely cracks on the surface seen in the SE image, rather than existence of Ga rich areas.

4.2.4 Photoluminescence

Room temperature photoluminescence (RT-PL) was measured from all of the bulk samples. However, only the high temperature grown sample showed efficient PL emission over a limited area corresponding to a As/Ga flux ratio range near the stoichiometric value (see Figure 4.20). The suppressed PL efficiency of the lower growth temperature samples is indicative of the incorporation of non-radiative defects into the lattice. All of the PL results presented in this chapter were taken from the regrown high growth temperature sample, which was cut specifically to accommodate the small sample stage inside the LT-PL cryostat chamber.

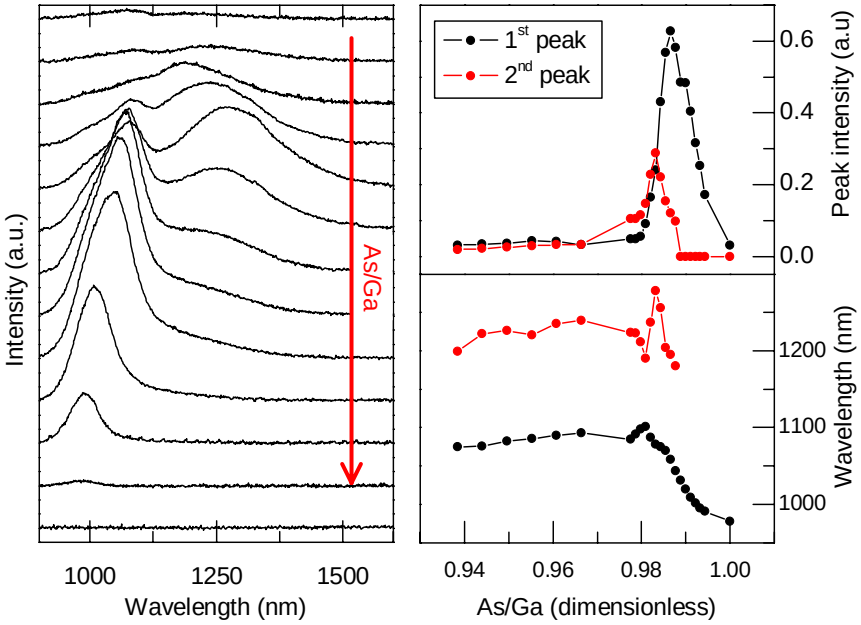

Figure 4.20 PL spectra and their corresponding peak intensities and positions as a function of the As/Ga flux ratio.

The RT-PL spectra show two distinct peaks corresponding to wavelengths of ~1100 nm and ~1200 nm, referred to 1st and 2nd peak in Figure 4.20, respectively. The shorter wavelength peak can be ascribed to band edge PL emission from the high Bi-fraction component of the double layer structure using the mVBAC model. The reason for the non-existent PL at the lower wavelengths, which would correspond to band edge PL from the low Bi-fraction component, could be explained by many factors. Firstly, as the carriers are more likely to recombine through the lowest possible states, diffusion of carries towards the high Bi-fraction layer and subsequent recombination is favorable. Secondly, the defect environment in each of the layers could be significantly different, i.e. the higher Bi layer could have less non-radiative defects and therefore emit more PL. Thirdly, albeit more tentatively, the high Bi-fraction layer could be the topmost layer and would experience more optical excitation due to the high optical absorption coefficient of GaAs (at the used excitation wavelength).

The PL intensity behavior with respect to the As/Ga flux ratio is explained by the surface composition and defect incorporation. At sub-stoichiometric values, the formed metallic droplets absorb and reflect light efficiently, lowering the overall PL efficacy. Simultaneously, the rough surface topology around the droplets (due to the droplet trails, for example) results in additional scattering losses. Additionally, the PL is also influenced by the defect environment and alloy inhomogeneity, although it is uncertain how exactly. At above stoichiometric As/Ga values, the native defect incorporation (see chapter 2.2) due to excess As quickly kills off the PL. The optimal PL efficiency is therefore near the stoichiometric range where losses related to the surface composition and defect density are minimized. Here, the PL is maximized at slightly below stoichi-

ometric conditions. In fact, the areas corresponding to the PL intensity maximum do show low density pure Ga droplets based on SEM measurements.

The long wavelength emission cannot be justified with simple band gap emission, as it would require the existence of higher Bi-fraction areas than detected by HRXRD. Similar sub-gap PL peaks are widely reported in literature [30, 37, 59, 60, 65, 66]. Most of the literature resolves these peaks' origin to be from localized states which arise due to Bi clustering (Bi dimers, trimers and so on), fluctuations in the alloy composition or defects (either impurity or Bi related). These localized states are simply electronic states which are spatially confined in the semiconductor lattice to a small area. Such states arise from local perturbations of the periodic potential of the lattice, which subsequently are caused by the aforementioned deviations from the ideal lattice structure. The PL emission from such states exhibit well-known temperature properties which are distinct from the ideal delocalized state emission (e.g. band edge emission). Therefore, to examine if the long wavelength emission shown in Figure 4.20 originates from localized states, a series of temperature dependent measurements were made.

A series of LT-PL measurements were taken from the same sample as in Figure 4.20 from an area where the long wavelength emission was dominant. The spectra are comprised in Figure 4.21. Increasing the temperature shifts the PL emission maximum to the long wavelength side. This indicates that the thermal occupation of the localized states increases with temperature, as expected due to the increased thermal energy, which enables more carriers to migrate to the localized states and recombine there. Additionally, the temperature evolution of the PL emphasizes that the spectra consists of an envelope of multiple peaks rather than a single peak.

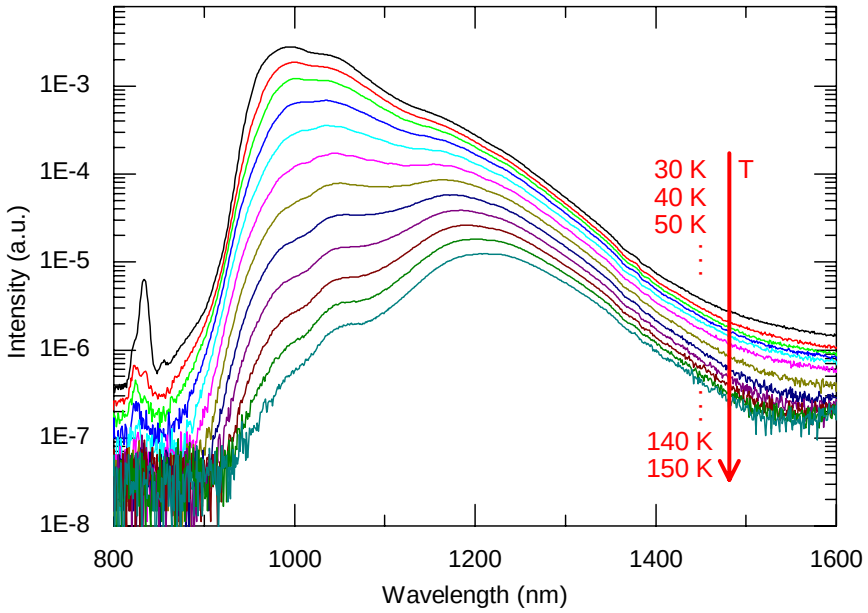

Figure 4.21 Temperature dependent LT-PL measurement series of the sample in Figure 4.20 from an As-limited area.

To show that the long wavelength component has a temperature dependence corresponding to that of a localized state, an accurate peak position is required. However, the estimation of peak positions manually from the broad shoulder is difficult. To combat this, each of the spectra was fitted with three individual Gaussians. Gaussian distributions are typically used to fit PL spectra of compound semiconductors, as the PL profiles of such compounds are dominated by inhomogeneous broadening due to stochastic compositional modulation. The envelope of the Gaussians was observed to fit exactly to that of the PL spectra. Examples of the fitted spectra are shown in Figure 4.22. The peak positions of the Gaussians are also compiled in the same figure, together with the manually picked peak positions of the RT-PL measurement.

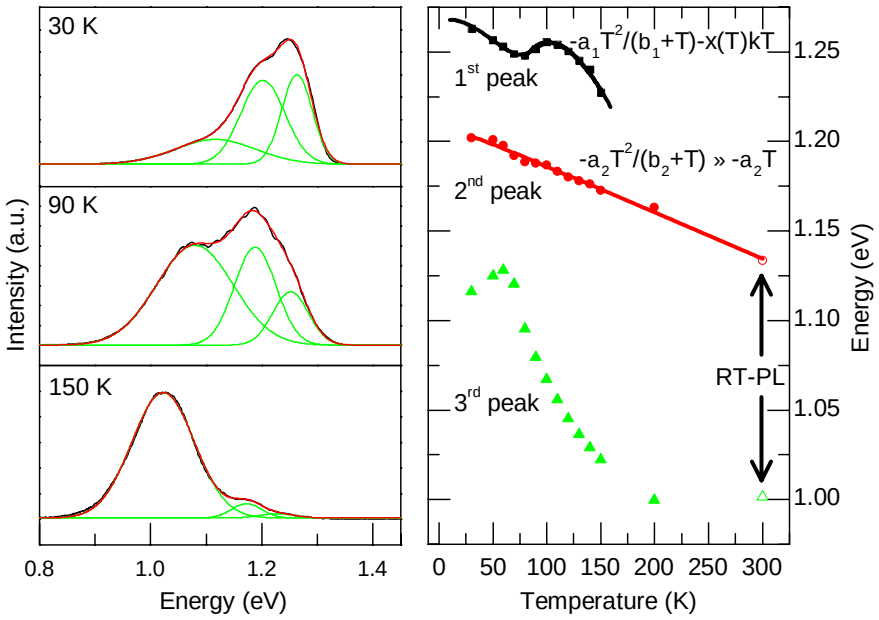

Figure 4.22 Examples of the fitted Gaussians to the spectra shown in Figure 4.21 and their respective peak positions as a function of temperature. On the left hand side of the graph the raw data is in black and the envelope of the individual Gaussians (green) is in red.

Figure 4.22 shows that two of the peaks have nonlinear and non-monotonous dependencies on temperature, which deviate from expected band gap temperature dependence determined by Varshni's law. For the 1st peak, the "S-shaped" behavior is a well-understood phenomenon for localized states which arises from the redistribution of carrier population at the localized states. At low temperature, the carriers are randomly distributed in all of the localized states. Increasing the temperature allows for the carriers to hop to the lowest possible sates, resulting in redshift. Further increase of the temperature results in carriers being thermally excited out from these states to more shallow states, causing blueshift. At sufficiently high temperatures the band-gap shrinkage (redshift) starts to dominate. For the 1st peak this trend is apparent and, in Figure 4.22, a model consistent with localized states formulated in references [67, 68] fits to the data well. At higher temperature range of above ~80 K, the model simplifies to an analytic dependency of $x(T)kT \approx \sigma^2/kT$ where $\sigma \approx 38$ meV, consistent with a band-tail-state emission model proposed by Eliseev et al. [69]. However, for the case of the 3rd peak the initial redshift is not visible, possibly due to the limited temperature range used here. In any case, the non-monotonous temperature dependence of the 3rd peak does not follow band edge behavior. Interestingly, the 3rd peak shows a rapid and anomalous temperature dependence at the high temperature range. This approximately exponential redshift of emission energy could be tentatively explained by the carrier population shifting rapidly due to the hopping probability increasing (exponentially) with temperature. Due to the scope of this work however, any further analysis is omitted here.

The origin of the 1st peak is unclear. Although it displays clear localized nature, it emits PL at an energy which is above the band edge emission (ascribed here to the 2nd peak), implying that the shallow localized state is below the valence band edge (the localized states here are assumed to be located near the valence band due to the location of Bi induced levels). The HRXRD spectra at the location of the measurement is too degraded to accurately say if the structure has a double layer composition profile, which would enable a layer with a lower Bi composition that could facilitate these localized states. Alternatively, the degraded HRXRD profile suggests an inhomogeneous composition profile, which would similarly enable the 1st peak's emission. The intensity behavior of the 1st peak supports this reasoning. At very low temperatures, the injected carriers are effectively frozen to their individual localized states and PL emitted through all of the possible states. When increasing the temperature, the carriers migrate from the shallow localized states (at the low Bi areas) to the deeper states (at the high Bi areas). The shallow states are therefore quickly vacated and recombination is dominated by the deeper states, as seen in Figure 4.21.

As mentioned previously, the 2nd peak in Figure 4.21 is ascribed to band edge emission, due to its more traditional temperature dependence (Varshni's equation fitted in Figure 4.21). Its peak position and intensity in relation to the lowest energy peak also corresponds well with the RT-PL measurements. It is also noted that the absolute thermal coefficient, $\alpha_2 \approx 0.26$ meV/K, of this peak would fit well with the data in Figure 2.3.

4.3 Characterization of GaAsBi quantum wells

Due to the complex dependencies of the GaAsBi bulk layer properties with respect to the growth parameters, the study of GaAsBi quantum wells (QW) in this work is limited only to simple single quantum well structures. Additionally, as only the highest temperature grown bulk layer showed efficient PL at room temperature, the QWs in this work were exclusively grown at the highest temperature of ~370 °C. This choice of growth temperature was motivated by the fact that QW based laser devices require good optical quality for efficient operation. To draw more similarities between the grown QWs and bulk structures, the nominal Bi-% was chosen to be the same for the QWs. The estimated Bi-fraction based on flux measurements was ~4.6 %. The nominal growth rate for the QW structures was also the same as for the bulk structures.

The growth of GaAsBi QWs, or in fact any GaAs/GaAsBi heterostructures, requires large temperature ramps to enable Bi incorporation into the active layers. During the ramps, growth of the cladding layers can either be interrupted or continued. Growth interruptions can lead to impurities accumulating on the growth surface resulting in poorer optical quality whereas continuing the growth during the ramps leads to gradients in materials properties due to the changing growth temperature. Conversely to the bulk samples, the QWs in this work were grown using the continuous growth scheme in

an attempt to optimize the optical quality of the samples. This choice was partly based on previous QW growth experiments (with substrate rotation), which indicated better PL efficiency for structures that were grown continuously. A detailed schematic of the growth process for the QWs is shown in Figure 4.23.

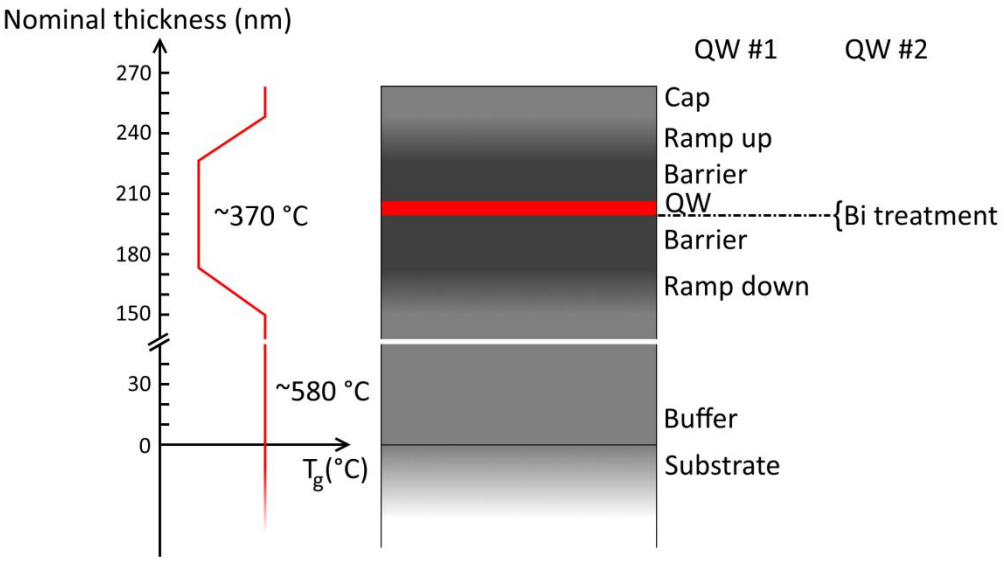

Figure 4.23 Schematic of the GaAsBi QW structures grown for this work. The labels on the right represent the different MBE growth steps. For QW #2 the growth steps were the same as QW #1 with the exception of the additional Bi treatment before the start of the QW layer.

The stationary growth for the QWs was enabled at the start of the first barrier layer (see Figure 4.23) to produce symmetric structures in terms of the barrier thicknesses and quality. Correspondingly, the substrate was kept stationary after the growth of the QW for the capping layers. At the same time as the rotation was stopped, the As flux was adjusted to enable Bi incorporation. This premature reduction in the As flux would reduce the amount of defect incorporation in the first barrier (grown at low temperature) while simultaneously give time for the As flux to stabilize. As for the bulk layers, the nominal As flux was set to correspond to a stoichiometric As/Ga flux ratio at the center of the wafer based on flux measurements. At the start of the ramp up layer, the As flux was readjusted to the same value as used in the buffer layer. This was done to prevent surface degradation at the higher growth temperature of the GaAs capping layer.

Two different QW samples, referred to as QW #1 and QW #2, are studied in this work. They were grown with exactly the same growth parameters and steps with the exception of QW #2 having a Bi treatment step before the start of the QW layer growth (see Figure 4.23). The purpose of the Bi treatment is to saturate the Bi coverage and wetting layer, which will enable a more abrupt change in composition together with improved compositional uniformity. For the Bi treatment step, the growth was interrupted with the

Bi shutter kept open. The Bi treatment lasted for ~50 s, which was equivalent to the time it took to grow the nominally ~7 nm thick QW layer.

4.3.1 Structural properties

The HRXRD spectra measured from the QWs are shown in Figure 4.24. At first sight, the structural quality and composition of the QWs seems to have better tolerance on the As/Ga flux ratio in comparison to the bulk layer (cf. Figure 4.15). However, as the spectra are influenced by all the components of the QW structure, it is difficult to estimate the real Bi composition or structural quality of the QW itself. Moreover, if the Bi incorporation is as complex as the bulk samples suggests and considering the growth is continuous after the QW layer with additional Bi being able to incorporate into the barrier, the Bi composition profile is expected to deviate significantly from the nominal case (see Figure 4.23). This uncertainty in the composition profile together with the complex strain profiles in the cladding layers, makes quantitative analysis by HRXRD simulations difficult. For example, choice of the simulation model affects the QW composition and thickness given by the optimal fit and multiple different models can be fitted with low amount of error. Furthermore, recent TEM measurements from previously grown GaAsBi QW samples (with substrate rotation) show significant compositional non-uniformity in the growth direction as well as laterally.

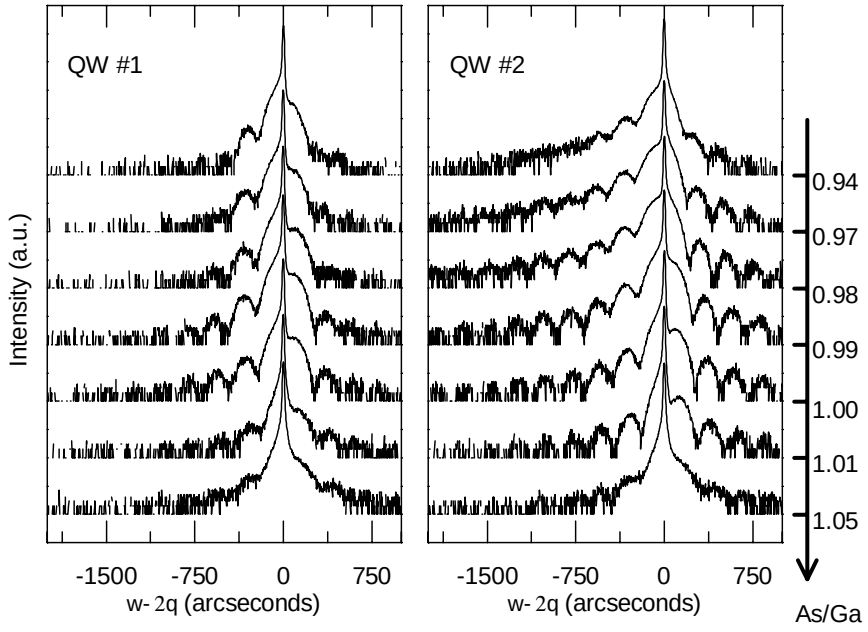

Figure 4.24 HRXRD measurements taken from the QW samples. The spectra which lie horizontally side-by-side were taken from the same locations on both of the wafers and correspond approximately to the same As/Ga values, which are marked on the right hand side of the graph.

Some qualitative information can be inferred from the HRXRD measurements. Overall, the strain in QW #2 is higher than QW #1. This is explained by the additional Bi atoms provided by the Bi treatment step. The Bi atoms from the Bi treatment step remain on the growth surface up to the start of the QW layer (due to the low desorption rate even at a growth temperature of ~370 °C [14]) and subsequently incorporate into the QW layer. Using the simplest possible simulation model (single homogeneous QW layer with an ideal GaAs capping layer), the HRXRD fits at the stoichiometric As/Ga value give roughly twice the amount of Bi incorporated in the QW layer for QW #2. This result reflects the effect of the Bi treatment layer well, due to the total amount of Bi offered for QW #2 being double that of QW #1.

Some similarities exist with the bulk layers. Highest quality spectra are achieved at the stoichiometric range, evidenced by the amount of visible thickness fringes. At below stoichiometric values, the fringes get less clear implying non-uniformity in composition and poor interfacial quality. Similar behavior is seen in the As-rich regime as well, with the addition of reduced strain, and therefore Bi composition, as in the bulk layers.

The surface quality of QW #1 was determined in detail by SEM and AFM measurements. The measurements of QW #2's surface quality are omitted here, due to the observation that the Bi treatment layer had negligible effects on the surface quality. This is somewhat expected due to the amount of Bi not being significantly larger in terms of Bi droplet formation and due to the fact that during the high temperature capping layer any accumulated surface Bi is evaporated. QW #1 is therefore thought of as a representative of both of the samples in terms of surface properties.

Figure 4.25 shows a series of AFM measurements from the As-limited regime to the stoichiometric regime. At the As-limited regime, primarily Ga droplets are formed (due to the low amount of Bi offered in comparison to the bulk samples) in the growth of the low temperature barriers and QW layer. Subsequently to the growth of the low temperature layers, the temperature and As pressure are increased to values corresponding optimal GaAs growth for the capping layer. This growth parameters change results in two effects. Firstly, the accumulated surface Bi is forced out due to increased temperature and As flux. Secondly, the Ga droplets are consumed by the increased As flux. The surface features seen in Figure 4.25a are presumably formed from the consumption of the Ga droplets. A part of these elevated features have cavities in the center, resembling quantum ring structures. GaAs quantum rings are manufactured by Ga deposition and subsequent As irradiation, which would explain the similar morphology seen here. The features are elongated in the [110] direction, corresponding to the orientation of the droplet trails in Figure 4.18. From a device engineering point of view, the surface quality at the As-limited regime is poor even for this single QW structure. Not only would real MQW devices have cumulative effects in terms of the surface features, but also would result in non-uniform QW positioning.

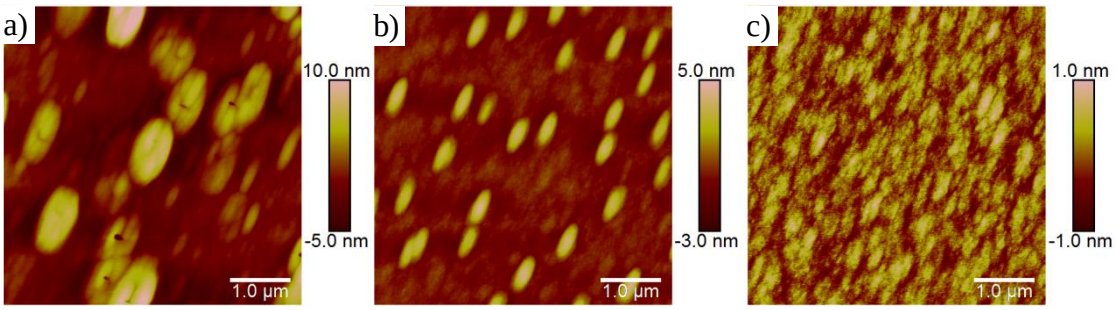

Figure 4.25 AFM measurements taken from the As-limited side of QW #1. The a, b and c images are from locations on the wafer which correspond to As/Ga flux ratio values of 0.98, 1.00 and 1.02, respectively.

At the stoichiometric and above As/Ga flux values, where droplets do not accumulate, the surface is smooth as expected. Accumulated surface Bi at the As-rich regime (cf. Figure 4.19) is not detected, which is consistent with the bulk sample and it is expected that any surplus Bi accumulated at lower temperatures would evaporate during the high temperature capping layer as well. The surface roughness does not significantly improve with increasing the As/Ga flux ratio above stoichiometric values (see Figure 4.28), as expected due to the high As overpressure used for the capping layer.

4.3.2 Photoluminescence

Compilation of the RT-PL results of QW #1 is shown in Figure 4.26. The results echo the PL behavior of the high temperature grown bulk layer. At the stoichiometric range the PL emission is maximized and any deviation from this value quickly kills off the PL. The PL spectra of QW #1 show a single Gaussian shaped peak at around ~1150 nm. The reason for the small dip in wavelength at the below stoichiometric range is unclear. Considering that the sample has only a single QW, the full width at half maximum (FWHM) value is large at ~180 meV (seemingly independent of the As/Ga value), indicating fluctuations in QW thickness and/or Bi composition.

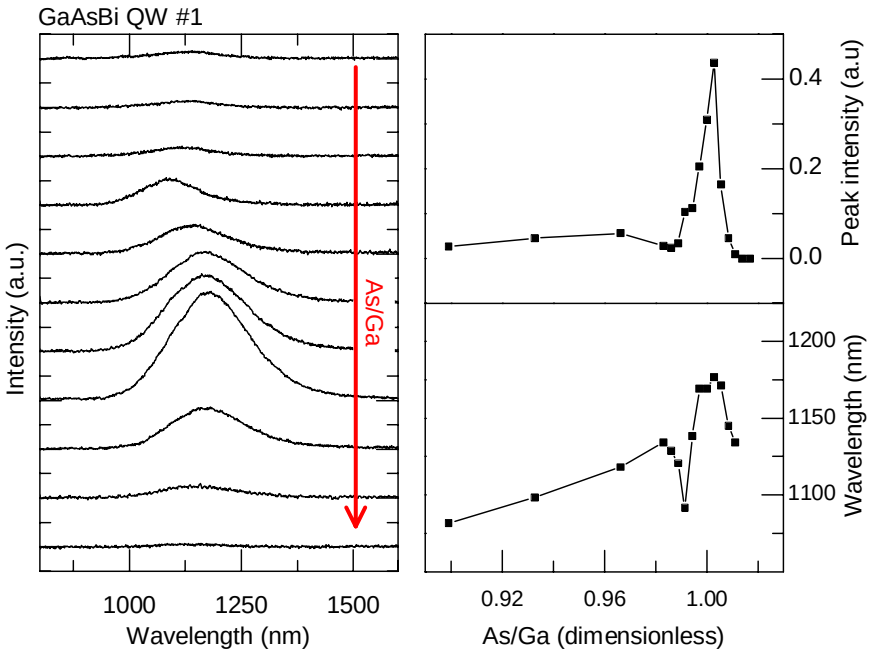

Figure 4.26 RT-PL spectra measured from QW #1 and their corresponding peak intensities and wavelengths as a function of the As/Ga flux ratio.

Figure 4.27 shows the same RT-PL compilation for QW #2, which shows a few distinct features in comparison to QW #1. Firstly, the PL emission intensity extends well into the As-limited range. This could be explained through either reduced defect density (possibly due to the increased Bi composition), improved confinement (more abrupt interface and increased Bi composition) or a combination of these factors. In any case, this discrepancy highlights the importance of the choice in MBE growth steps. Secondly, the narrow growth window with high PL emission of QW #1 is significantly wider for QW #2 (by a factor of ~4), making device manufacture more forgiving. Conversely however, the emission wavelength of QW #2 is a bit more sensitive to the As/Ga value, probably due to a difference in Bi incorporation properties due to the additional Bi provided. Similar reasoning follows for the discrepancies in the wavelength behavior at the As-limited regime. Additionally, the absolute PL signal maximum is worse for QW #2, which again can be explained by the aforementioned factors. It is important to note that the Bi treatment does involve a growth interruption at low temperature, which influences the overall PL efficiency through additional impurity incorporation during the interruption. The FWHM for QW #2 is not significantly different at ~218 meV (value approximated by Gaussian fits). However, the PL emission profiles of QW #2 show slight deviation from the ideal Gaussian behavior of QW #1. Specifically, at the stoichiometric As/Ga range the profiles are asymmetric exhibiting a short wavelength shoulder. This could be conceived as consistency with the bulk PL results, but unfortunately as there are many other viable reasons to explain this behavior, any conclusions are omitted here.

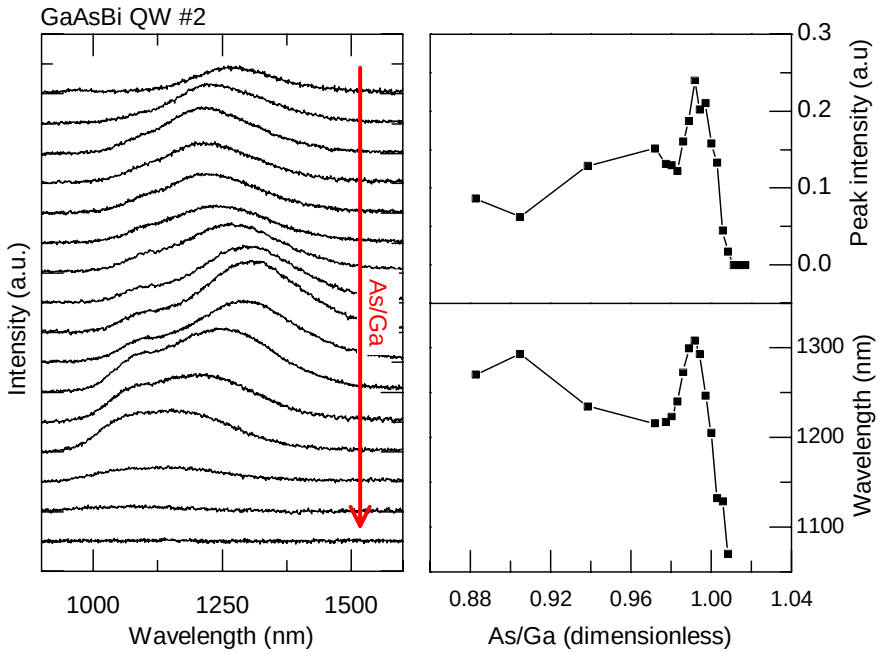

Figure 4.27 RT-PL spectra measured from QW #2 and their corresponding peak intensities and wavelengths as a function of the As/Ga flux ratio.

From the perspective of GaAsBi laser device engineering, it is important to examine how the surface roughness behaves in relation to PL emission, as both are critical factors in device performance. To this end, the roughness and PL intensity measured from QW #1 are compiled in Figure 4.28 as a function of the As/Ga flux ratio.

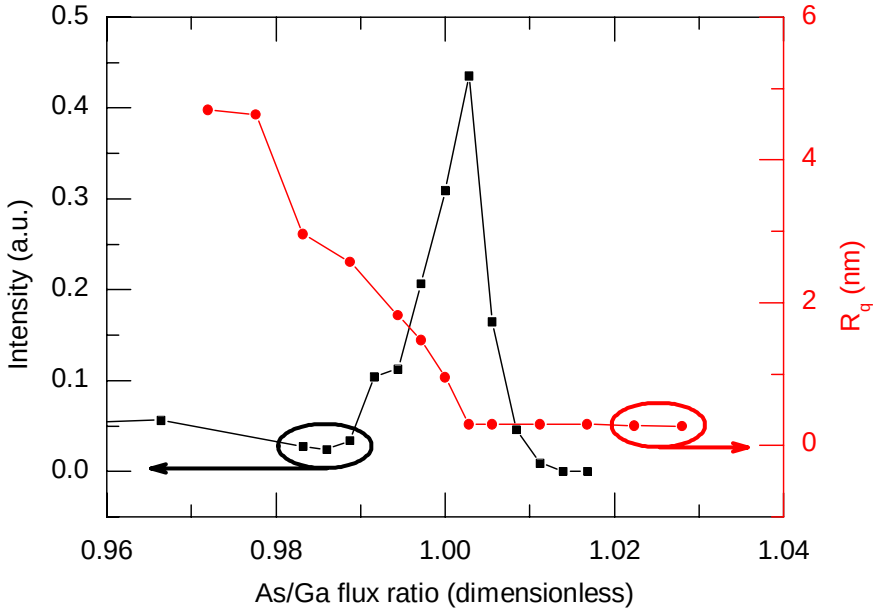

Figure 4.28 QW #1's RT-PL peak intensity and surface roughness as a function of the As/Ga flux ratio. The root mean square roughness values (R_q) were determined by AFM measurements from surface areas of 5×5 µm².

Figure 4.28 shows that there is a clear optimal As/Ga value (just above the stoichiometric value) with maximized PL intensity and low surface roughness. The narrow optimal growth window demonstrates the challenges in the growth of GaAsBi devices while showing it is possible to achieve good optical quality even for such low temperature grown material. Additionally, this result reinforces the usefulness of in-situ surface roughness detection (e.g. light scattering techniques) for GaAsBi growth, as the onset of surface roughness coincides with the PL maximum.

5. CONCLUSIONS

In summary of the work conducted in this thesis, a research methodology for stationary MBE growth has been developed and applied to determine the properties of GaAsBi layers with respect to their growth parameters. The results with regard to GaAsBi growth are generally in agreement with the literature, although a number of new interesting observations have been presented here. Most importantly, spontaneous changes in the Bi composition have been observed at specific growth regimes. The incorporation of Bi into GaAs, structural properties as well as optical quality have been shown to be extremely sensitive to the As/Ga flux ratio, highlighting the challenges in GaAsBi growth.

Growth of GaAsBi at low temperatures enables a larger growth window with efficient Bi incorporation and good structural quality, but native defect incorporation impairs the optical quality. Growth at elevated temperatures reduces Bi incorporation and pins down the growth window to the stoichiometric range. However, at this high temperature and stoichiometric As/Ga regime the defect incorporation is diminished and so the material shows efficient photoluminescence. Reducing the As/Ga ratio below stoichiometric influences crystalline quality negatively and induces droplet formation. Structural disorder at this range is also reflected by the PL spectrum being dominated by mid-gap states.

The results regarding GaAsBi QWs in this work echo the behavior of the bulk layers. The growth window for good optical quality QWs is limited to the high growth temperature and stoichiometric As/Ga flux ratio range. Additionally, the influence of the choices in MBE growth steps for QW growth was examined. Namely, adding a pure Bi deposition step before the start of the QW influenced the overall structural and optical properties. In terms of device engineering, the optical quality of the QWs was found to be promising.

5.1 Future work

Only a narrow growth parameter space has been explored in this thesis. Work involving stationary growth of GaAsBi at different nominal Bi fluxes or growth rates will likely yield interesting results and further advance the understanding of Bi incorporation into GaAs. Moreover, the effect of other still relatively unexplored growth parameters like the choice of As species or substrate crystal orientation should be studied. Additionally, the effects of post growth processing, such as thermal annealing, could be studied from

the grown samples with the benefit of mitigating run-to-run variation of the processing variables.

For MBE research, the stationary growth method offers a way of reducing the amount of growths and improves reproducibility of samples. Therefore, this methodology could be applied to the research of other materials where material properties are extremely sensitive to the growth parameters. For example, other dilute bismides, such as GaSbBi or InSbBi, could be potential candidates. In terms of device manufacture, stationary growth has obvious downsides in not being able to produce layers with uniform thickness across the whole wafer. However, optimal growth parameters would be easier to achieve, thereby enabling high performance devices. Ideally, the Ga flux gradient should be minimized in growth of GaAsBi devices to minimize thickness variation across the wafer. This could be achieved by adjusting the manipulator orientation in growth, for example. Simultaneously, this would influence the overall As/Ga gradient over the wafer, and thus could be used to increase or decrease the observable As/Ga range. Nevertheless, for conventional rotated device growth, the results of these non-rotated growth structures could be used as a guide in finding the optimal growth parameters as well as a probing the maximal performance capabilities of devices.

The results of the sub-stoichiometric As/Ga ratio growth regime demonstrate that this regime should be studied further. Generally, information given by HRXRD is often insufficient or ambiguous for quantitative analysis, due to the compositional changes and structural degradation. To this end, other research methods which give more accurate compositional information for these structures, such as Rutherford backscattering spectrometry or TEM, are critical in understanding the Bi incorporation properties. Further studies on the underlying mechanics of double layer formation would also require additional in-situ capabilities of the MBE reactor.

REFERENCES

[1] M. Henini, Molecular Beam Epitaxy: From Research to Mass Production, Elsevier, 2012.

[2] R. F. C. Farrow, Molecular Beam Epitaxy, Elsevier, 1995.

[3] S. Tixier, M. Adamcyk, T. Tiedje, S. Francoeur, A. Mascarenhas, P. Wei and F. Schiettekatte, "Molecular beam epitaxy growth of GaAsBi," *Applied Physics Letters,* vol. 82, p. 2245, 2003.

[4] S. Francoeur, M.-J. Seong, A. Mascarenhas, S. Tixier, M. Adamcyk and T. Tiedje, "Band gap of GaAsBi, 0<x<3.6%," *Applied Physics Letters,* vol. 82, p. 3874, 2003.

[5] X. Lu, D. A. Beaton, R. B. Lewis, T. Tiedje and Y. Zhang, "Composition dependence of photoluminescence of GaAsBi alloys," *Applied Physics Letters,* vol. 95, p. 041903, 2009.

[6] M. Usman, C. A. Broderick, A. Lindsay and E. P. O'Reilly, "Tight-binding analysis of the electronic structure of dilute bismide alloys of GaP and GaAs," *Physical Review B,* vol. 84, p. 245202, 2011.

[7] B. Fluegel, S. Francoeur and A. Mascarenhas, "Giant Spin-Orbit Bowing in GaAsBi," *Physical Review Letters,* vol. 97, p. 067205, 2006.

[8] Z. Batool, K. Hild, T. J. C. Hosea, X. Lu, T. Tiedje and S. J. Sweeney, "The electronic band structure of GaBiAs/GaAs layers: Influence of strain and band anti-crossing," *Journal of Applied Physics,* vol. 111, p. 113108, 2012.

[9] F. W. Smith, A. R. Calawa, C.-L. Chen, M. J. Manfra and L. J. Mahoney, "New MBE buffer used to eliminate backgating in GaAs MESFETs," *IEEE Electron Device Letters,* vol. 9, p. 77, 1988.

[10] S. Gupta, M. Y. Frankel, J. A. Valdmanis, J. F. Whitaker, G. A. Mourou, F. W. Smith and A. R. Calawa, "Subpicosecond carrier lifetime in GaAs grown by molecular beam epitaxy at low temperatures," *Applied Physics Letters,* vol. 59, p. 3276, 1991.

[11] J. M. Kim, Y. T. Lee, J. D. Song and J. H. Kim, "Electrical properties and ultrafast photo-response of InGaAs/InP grown by low-temperature molecular beam epitaxy

with a GaAs decomposition source," *Journal of Crystal Growth,* vol. 265, p. 8, 2004.

[12] K. Bertulis, A. Krotkus, G. Aleksejenko, V. Pacebutas, R. Adomavicius, G. Molis and S. Marcinkevicius, "GaBiAs: A material for optoelectronic terahertz devices," *Applied Physics Letters,* vol. 88, p. 201112, 2006.

[13] K. Oe and H. Okamoto, "New semiconductor alloy GaAsBi grown by metal organic vapor phase epitaxy," *Japanese Journal of Applied Physics,* vol. 37, p. L1283, 1998.

[14] A. J. Noreika, W. J. Takei, M. H. Francombe and C. E. C. Wood, "Indium antimonide-bismuth compositions grown by molecular beam epitaxy," *Journal of Applied Physics,* vol. 53, p. 4932, 1982.

[15] M. K. Rajpalke, W. M. Linhart, M. Birkett, K. M. Yu, D. O. Scanlon, J. Buckeridge, T. S. Jones, M. J. Ashwin and T. D. Veal, "Growth and properties of GaSbBi alloys," *Applied Physics Letters,* vol. 103, p. 142106, 2013.

[16] Y. Gu, K. Wang, H. F. Zhou, L. Y. Zhang, C. Z. Kang, M. J. Wu, W. W. Pan, P. F. Lu, Q. Gong and S. M. Wang, "InPBi single crystals grown by molecular beam epitaxy," *Nature Scientific Reports,* vol. 4, p. 5449, 2014.

[17] R. B. Lewis, M. Masnadi-Shirazi and T. Tiedje, "Growth of high Bi concentration GaAsBi by molecular beam epitaxy," *Applied Physics Letters,* vol. 101, no. 8, p. 082112, 2012.

[18] Z. Pan, L. Li, W. Zhang, X. Wang, Y. Lin and R. Wu, "Growth and characterization of GaInNAs/GaAs by plasma-assisted molecular beam epitaxy," *Journal of Crystal Growth,* Vols. 227-228, p. 516, 2001.

[19] X. Liu, A. Prasad, J. Nishio, E. R. Weber, Z. Liliental-Weber and W. Walukiewicz, "Native point defects in low-temperature grown GaAs," *Applied Physics Letters,* vol. 67, p. 279, 1995.

[20] A. Suda and N. Otsuka, "Arsenic flux dependence of incorporation of excess arsenic in molecular beam epitaxy of GaAs at low temperature," *Applied Physics Letters,* vol. 73, p. 1529, 1998.

[21] M. Lagadas, M. Androulidaki, Z. Hatzopoulos and M. Calamiotou, "Dependence of arsenic antisite defect concentration and two dimensional growth mode on LT GaAs growth conditions," *Microelectronic Engineering,* vol. 1998, p. 581, 1998.

[22] L. G. Lavrent'eva, M. D. Vilisova, I. A. Bobrovnikova, S. E. Toropov, V. V. Preobrazhenskii, B. R. Semyagin, M. A. Putyato and V. V. Chaldyshev, "Excess arsenic and point defects in GaAs grown by molecular beam epitaxy at low temperatures," *Journal of Structural Chemistry,* vol. 45, p. S88, 2004.

[23] N. Elayech, H. Fitouri, Y. Essouda, A. Rebey and B. E. Jani, "Thermodynamic study of the ternary system gallium-arsenic-bismuth," *Physica Status Solidi C,* vol. 12, p. 138, 2015.

[24] X. Lu, D. A. Beaton, R. B. Lewis, T. Tiedje and M. B. Whitwick, "Effect of molecular beam epitaxy growth conditions on the Bi content of GaAsBi," *Applied Physics Letters,* vol. 92, p. 192110, 2008.

[25] K. Takahiro, K. Kawatsura, K. Oe and F. Nishiyama, "Structural characterization of GaAsBi alloy by Rutherford backscattering spectrometry combined with the channeling technique," *Journal of Electronic Materials,* vol. 32, p. 34, 2003.

[26] M. J. Seong, S. Francoeur, S. Yoon, A. Mascarenhas, S. Tixier, M. Adamcyk and T. Tiedje, "Bi-induced vibrational modes in GaAsBi," *Superlattices and Microstructures,* vol. 37, p. 394, 2005.

[27] F. Bastiman, A. R. B. Mohmad, J. S. Ng, J. P. R. David and S. J. Sweeney, "Non-stoichiometric GaAsBi/GaAs (100) molecular beam epitaxy growth," *Journal of Crystal Growth,* vol. 338, p. 57, 2012.

[28] G. Vardar, S. W. Paleg, M. V. Warren, M. Kang, S. Jeon and R. S. Goldman, "Mechanisms of droplet formation and Bi incorporation during molecular beam epitaxy of GaAsBi," *Applied Physics Letters,* vol. 102, p. 042106, 2013.

[29] A. J. Ptak, R. France, D. A. Beaton, K. Alberi, K. Simon, A. Mascarenhas and C.-S. Jiang, "Kinetically limited growth of GaAsBi by molecular-beam epitaxy," *Journal of Crystal Growth,* vol. 338, p. 107, 2011.

[30] A. R. Mohmad, F. Bastiman, C. J. Hunter, R. D. Richards, S. J. Sweeney, J. S. Ng, J. P. R. David and B. Y. Majlis, "Localization effects and band gap of GaAsBi alloys," *Physica Status Solidi B,* vol. 251, p. 1276, 2014.

[31] R. D. Richards, F. Bastiman, C. J. Hunter, D. F. Mendes, A. R. Mohmad, J. S. Roberts and J. P. R. David, "Molecular beam epitaxy growth of GaAsBi using As2 and As4," *Journal of Crystal Growth,* vol. 390, p. 120, 2014.

[32] M. Henini, J. Ibanez, M. Schmidbauer, M. Shafi, S. V. Novikov, L. Turyanska, S. I. Molina, D. L. Sales, M. F. Chisholm and J. Misiewicz, "Molecular beam epitaxy

of GaBiAs on (311)B GaAs substrates," *Applied Physics Letters,* vol. 91, p. 251909, 2007.

[33] Z. Chine, H. Fitouri, I. Zaied, A. Rebey and B. E. Jani, "Photoreflectance and photoluminescence study of annealing effects on GaAsBi layers grown by metalorganic vapor phase epitaxy," *Semiconductor Science and Technology,* vol. 25, p. 065009, 2010.

[34] G. Pettinari, A. Patane, A. Polimeni, M. Capizzi, X. Lu and T. Tiedje, "Bi-induced p-type conductivity in nominally undoped Ga(AsBi)," *Applied Physics Letters,* vol. 100, p. 092109, 2012.

[35] K. Alberi, J. Wu, W. Walukiewicz, K. M. Yu, O. D. Dubon, S. P. Watkins, C. X. Wang, X. Liu, Y.-J. Cho and J. Furdyna, "Valence-band anticrossing in mismatched III-V semiconductor alloys," *Physical Review B,* vol. 75, p. 045203, 2007.

[36] C. A. Broderick, M. Usman, S. J. Sweeney and E. P. O'Reilly, "Band engineering in dilute nitride and bismide semiconductor lasers," *Semiconductor Science and Technology,* vol. 27, p. 094011, 2012.

[37] V. Bahrami-Yekta, T. Tiedje and M. Masnadi-Shirazi, "MBE growth optimization for GaAsBi and dependence of photoluminescence on growth temperature," *Semiconductor Science and Technology,* vol. 30, p. 094007, 2015.

[38] Y. Tominaga, K. Oe and M. Yoshimoto, "Temperature-insensitive photoluminescence emission wavelength in GaAsBi/GaAs multiquantum wells," *Physica Status Solidi C,* vol. 8, p. 260, 2011.

[39] G. Pettinari, M. Capizzi and A. Polimeni, "Carrier masses and band-gap temperature sensitivity in Ga(AsBi) alloys," *Semiconductor Science and Technology,* vol. 30, p. 094002, 2015.

[40] D. G. Cooke, F. A. Hegmann, E. C. Young and T. Tiedje, "Electron mobility in dilute GaAs bismide and nitride alloys measured by time-resolved terahertz spectroscopy," *Applied Physics Letters,* vol. 89, p. 122103, 2006.

[41] R. N. Kini, L. Bhusal, A. J. Ptak, R. France and A. Mascarenhas, "Electron Hall mobility in GaAsBi," *Journal of Applied Physics,* vol. 2009, p. 043705, 2009.

[42] R. N. Kini, A. J. Ptak, B. Fluegel, R. France, R. C. Reedy and A. Mascarenhas, "Effect of Bi alloying on the hole transport in the dilute bismide alloy GaAsBi,"

Physical Review B, vol. 83, p. 075307, 2011.

[43] D. A. Beaton, R. B. Lewis, M. Masnadi-Shirazi and T. Tiedje, "Temperature dependence of hole mobility in GaAsBi alloys," *Journal of Applied Physics,* vol. 108, p. 083708, 2010.

[44] A. Janotti, S.-H. Wei and S. B. Zhang, "Theoretical study of the effects of isovalent coalloying of Bi and N in GaAs," *Physical Review B,* vol. 65, p. 115203, 2002.

[45] S. Imhof, A. Thränhardt, A. Chernikov, M. Koch, N. S. Köster, K. Kolata, S. Chatterjee, S. W. Koch, X. Lu, S. R. Johnson, D. A. Beaton, T. Tiedje and O. Rubel, "Clustering effects in Ga(AsBi)," *Applied Physics Letters,* vol. 96, p. 131115, 2010.

[46] D. L. Sales, E. Guerrero, J. F. Rodrigo, P. L. Galindo, A. Yanez, M. Shafi, A. Khatab, R. H. Mari, M. Henini, S. Novikov, M. F. Chisholm and S. I. Molina, "Distribution of bismuth atoms in epitaxial GaAsBi," *Applied Physics Letters,* vol. 98, p. 101902, 2011.

[47] M. Wu, E. Luna, J. Puustinen, M. Guina and A. Trampert, "Observation of atomic ordering of triple-period-A and -B type in GaAsBi," *Applied Physics Letters,* vol. 105, p. 041602, 2014.

[48] A. G. Norman, R. France and A. J. Ptak, "Atomic ordering and phase separation in MBE GaAsBi," *Journal of Vacuum Science and Technology B,* vol. 29, p. 03C121, 2011.

[49] E. Luna, M. Wu, J. Puustinen, M. Guina and A. Trampert, "Spontaneous formation of nanostructures by surface spinodal decomposition in GaAsBi epilayers," *Journal of Applied Physics,* vol. 117, p. 185302, 2015.

[50] M. Wu, E. Luna, J. Puustinen, M. Guina and A. Trampert, "Formation and phase transformation of Bi-containing QD-like clusters in annealed GaAsBi," *Nanotechnology,* vol. 25, p. 205605, 2014.

[51] P. F. Fewster and C. J. Curling, "Composition and latticemismatch measurement of thin semiconductor layers by x-ray diffraction," *Journal of Applied Physics,* vol. 62, p. 4154, 1987.

[52] H. J. Queisser and C. S. Fuller, "Photoluminescence of Cu-doped gallium arsenide," *Journal of Applied Physics,* vol. 37, p. 4895, 1966.

[53] R. F. Egerton, Physical Principles of Electron Microscopy: An introduction to TEM, SEM, and AEM, Springer, 2005.

[54] N. A. Geisse, "AFM and combined optical techniques," *Materials Today,* vol. 12, no. 7-8, p. 40, 2009.

[55] N. J. Kawai, T. Nakagawa, T. Kojima, K. Ohta and M. Kawashima, "Arsenic passivation: A possible remedy for MBE growth-interruption problems," *Electronic Letters,* vol. 20, p. 47, 1984.

[56] J. K. Grepstad, H. Husby, A. Borg, B.-O. Fimland, R. W. Bernstein and R. Nyholm, "As capping of MBE-grown compound semiconductors; Novel opportunities to interface science and device fabrication," *Physica Scripta,* vol. T54, p. 216, 1994.

[57] J. Hilska, "Novel method for arsenic flux determination in molecular beam epitaxy," Bachelor of Science thesis, Tampere University of Technology, 2015. [Online]. Available: http://www.students.tut.fi/~hilska/BSc.pdf.

[58] VG Semicon, V80H-10 Molecular Beam Epitaxy System Operator's Manual, 2000.

[59] Y. I. Mazur, V. G. Dorogan, M. Benamara, M. E. Ware, M. Schmidbauer, G. G. Tarasov, S. R. Johnson, X. Lu, S.-Q. Yu, T. Tiedje and G. J. Salamo, "Effects of spatial confinement and layer disorder in photoluminescence of GaAsBi/GaAs heterostructures," *Journal of Physics D: Applied Physics,* vol. 46, p. 065306, 2013.

[60] A. R. Mohmad, F. Bastiman, C. J. Hunter, F. Harun, D. F. Reyes, D. L. Sales, D. Gonzalez, R. D. Richards, J. P. R. David and B. Y. Majlis, "Bismuth concentration inhomogeneity in GaAsBi bulk and quantum well structures," *Semiconductor Science and Technology,* vol. 30, p. 094018, 2015.

[61] D. F. Reyes, F. Bastiman, C. J. Hunter, D. L. Sales, A. M. Sanchez, J. P. R. David and D. González, "Bismuth incorporation and the role of ordering in GaAsBi/GaAs structures," *Nanoscale Research Letters,* vol. 9, p. 1, 2014.

[62] J. Puustinen, "Growth and characterization of GaAsBi structures by molecular beam epitaxy," Master of Science Thesis, Tampere University of Technology, 2014.

[63] M. Masnadi-Shirazi, D. A. Beaton, R. A. Lewis, X. Lu and T. Tiedje, "Surface reconstructions during growth of GaAsBi alloys by molecular beam epitaxy," *Journal of Crystal Growth,* vol. 338, p. 80, 2012.

[64] J. Wu, Z. M. Wang, A. Z. Li, M. Benamara, S. Li and G. J. Salamo, “Nanoscale footprints of self-running gallium droplets on GaAs surface,” *Public Library of Science ONE,* vol. 6, p. e20765, 2011.

[65] M. Beaudoin, R. B. Lewis, J. J. Andrews, V. Bahrami-Yekta, M. Masnadi-Shirazi, S. K. O'Leary and T. Tiedje, “Bandedge optical properties of MBE grown GaAsBi films measured by photoluminescence and photothermal deflection spectroscopy,” *Journal of Crystal Growth,* vol. 425, p. 245, 2015.

[66] M. Masnadi-Shirazi, R. B. Lewis, V. Bahrami-Yekta, T. Tiedje, M. Chicoine and P. Servati, “Bandgap and optical absorption edge of GaAsBi alloys with $0 < x < 17.8$ %,” *Journal of Applied Physics,* vol. 116, p. 223506, 2014.

[67] Z. Y. Xu, Z. D. Lu, Z. L. Yuan, X. P. Yang, B. Z. Zheng, J. Z. Xu, W. K. Ge, Y. Wang, J. Wang and L. L. Chang, “Thermal activation and thermal transfer of localized excitons in InAs self-organized quantum dots,” *Superlattices and Microstructures,* vol. 23, p. 381, 1998.

[68] Q. Li, S. J. Xu, W. C. Cheng, M. H. Xie, S. Y. Tong, C. M. Che and H. Yang, “Thermal redistribution of localized excitons and its effect on the luminescence band in InGaN ternary alloys,” *Applied Physics Letters,* vol. 2001, p. 1810, 79.

[69] P. G. Eliseev, “The red σ^2/kT spectral shift in partially disordered semiconductors,” *Journal of Applied Physics,* vol. 93, p. 5404, 2003.